



**AFRL-RX-WP-TP-2011-4421**

# **ATOMIC STRUCTURE OF $\text{Ca}_{40+x}\text{Mg}_{25}\text{Cu}_{35-x}$ METALLIC GLASSES (PREPRINT)**

**O.N. Senkov, D.B. Miracle, and C.F. Woodward**

**Metals Branch**

**Metals, Ceramics & NDE Division**

**Y.Q. Cheng**

**Johns Hopkins University**

**E.R. Barney**

**Rutherford Appleton Laboratory**

**DECEMBER 2011**

**Approved for public release; distribution unlimited.**

*See additional restrictions described on inside pages*

**STINFO COPY**

**AIR FORCE RESEARCH LABORATORY  
MATERIALS AND MANUFACTURING DIRECTORATE  
WRIGHT-PATTERSON AIR FORCE BASE, OH 45433-7750  
AIR FORCE MATERIEL COMMAND  
UNITED STATES AIR FORCE**

REPORT DOCUMENTATION PAGE					Form Approved OMB No. 0704-0188	
<p>The public reporting burden for this collection of information is estimated to average 1 hour per response, including the time for reviewing instructions, searching existing data sources, gathering and maintaining the data needed, and completing and reviewing the collection of information. Send comments regarding this burden estimate or any other aspect of this collection of information, including suggestions for reducing this burden, to Department of Defense, Washington Headquarters Services, Directorate for Information Operations and Reports (0704-0188), 1215 Jefferson Davis Highway, Suite 1204, Arlington, VA 22202-4302. Respondents should be aware that notwithstanding any other provision of law, no person shall be subject to any penalty for failing to comply with a collection of information if it does not display a currently valid OMB control number. <b>PLEASE DO NOT RETURN YOUR FORM TO THE ABOVE ADDRESS.</b></p>						
1. REPORT DATE (DD-MM-YY) December 2011		2. REPORT TYPE Journal Article Preprint		3. DATES COVERED (From - To) 01 October 2011 – 01 October 2011		
4. TITLE AND SUBTITLE ATOMIC STRUCTURE OF $\text{Ca}_{40+X}\text{Mg}_{25}\text{Cu}_{35-X}$ METALLIC GLASSES (PREPRINT)				5a. CONTRACT NUMBER In-house		
				5b. GRANT NUMBER		
				5c. PROGRAM ELEMENT NUMBER 61102F		
6. AUTHOR(S) O.N. Senkov, D.B. Miracle, and C.F. Woodward (AFRL/RXLM) Y.Q. Cheng (Johns Hopkins University) E.R. Barney (Rutherford Appleton Laboratory)				5d. PROJECT NUMBER 2303		
				5e. TASK NUMBER		
				5f. WORK UNIT NUMBER LM10512P		
7. PERFORMING ORGANIZATION NAME(S) AND ADDRESS(ES) Metals Branch (AFRL/RXLM) Metals, Ceramics & NDE Division Air Force Research Laboratory Materials and Manufacturing Directorate Wright-Patterson Air Force Base, OH 45433-7750 Air Force Materiel Command United States Air Force				8. PERFORMING ORGANIZATION REPORT NUMBER AFRL-RX-WP-TP-2011-4421		
9. SPONSORING/MONITORING AGENCY NAME(S) AND ADDRESS(ES) Air Force Research Laboratory Materials and Manufacturing Directorate Wright-Patterson Air Force Base, OH 45433-7750 Air Force Materiel Command United States Air Force				10. SPONSORING/MONITORING AGENCY ACRONYM(S) AFRL/RXLM		
				11. SPONSORING/MONITORING AGENCY REPORT NUMBER(S) AFRL-RX-WP-TP-2011-4421		
12. DISTRIBUTION/AVAILABILITY STATEMENT Approved for public release; distribution unlimited.						
13. SUPPLEMENTARY NOTES PAO Case Number: 88ABW 2011-5434; Clearance Date: 12 Oct 2011. Document contains color. Journal article submitted to <i>Physical Review B</i> .						
14. ABSTRACT The atomic structures of four $\text{Ca}_{40+X}\text{Mg}_{25}\text{Cu}_{35-X}$ ( $X = 0, 5, 10, \text{ and } 20 \text{ at.}\%$ ) ternary metallic glasses have been determined using a synergistic combination of neutron diffraction, quantum molecular dynamic (QMD) simulation and constrained reverse Monte Carlo modeling. The amorphous structure of these alloys can be described as close-packing of efficiently-packed Cu-centered clusters that have Ca, Mg and Cu atoms in the first coordination shells. Experimental evidence is given for the presence of Cu atoms in inter-cluster sites for the two most Cu-rich glasses. The close-packed arrangement of clusters is present only within length scale a length scale of $\sim 10 \text{ \AA}$ , providing a characteristic medium range order pre-peak at $Q \sim 1.2 \text{ \AA}^{-1}$ in the total scattering structure factors of these alloys. An average coordination number of 10 (with about 5-7 Ca, 2-3 Mg and 1-2 Cu atoms) is most common for the Cu-centered clusters. The average coordination numbers around Mg and Ca are 12-13 ( $\sim 6-8 \text{ Ca}$ , 3 Mg and 1-4 Cu) and 13-15 (7-9 Ca, 3-4 Mg, and 2-5 Cu), respectively, and they are composition dependent.						
15. SUBJECT TERMS bulk metallic glasses, atomic structure, short range order, medium range atomic order						
16. SECURITY CLASSIFICATION OF:			17. LIMITATION OF ABSTRACT: SAR	18. NUMBER OF PAGES 54	19a. NAME OF RESPONSIBLE PERSON (Monitor) Jonathan Spowart	
a. REPORT Unclassified	b. ABSTRACT Unclassified	c. THIS PAGE Unclassified			19b. TELEPHONE NUMBER (Include Area Code) N/A	

## Atomic Structure of $\text{Ca}_{40+X}\text{Mg}_{25}\text{Cu}_{35-X}$ Metallic Glasses

O.N. Senkov,<sup>1,\*</sup> Y.Q. Cheng,<sup>2</sup> D.B. Miracle,<sup>1</sup> E.R. Barney,<sup>3</sup> and C.F. Woodward<sup>1</sup>

<sup>1</sup> Air Force Research Laboratory, Wright Patterson Air Force Base, Ohio 45433, USA

<sup>2</sup> Department of Materials Science and Engineering, John Hopkins University, Baltimore, Maryland 21218, USA

<sup>3</sup> ISIS Facility, Rutherford Appleton Laboratory, Chilton, Didcot, OX11 0QX, UK.

\* Corresponding author, oleg.senkov@wpafb.af.mil. Telephone number: 937-255-4064.

### ABSTRACT

The atomic structures of four  $\text{Ca}_{40+X}\text{Mg}_{25}\text{Cu}_{35-X}$  ( $X = 0, 5, 10$ , and  $20$  at.%) ternary metallic glasses have been determined using a synergistic combination of neutron diffraction, quantum molecular dynamic (QMD) simulation and constrained reverse Monte Carlo modeling. The amorphous structure of these alloys can be described as close-packing of efficiently-packed Cu-centered clusters that have Ca, Mg and Cu atoms in the first coordination shells. Experimental evidence is given for the presence of Cu atoms in inter-cluster sites for the two most Cu-rich glasses. The close-packed arrangement of clusters is present only within length scale a length scale of  $\sim 10$  Å, providing a characteristic medium range order pre-peak at  $Q \sim 1.2$  Å in the total scattering structure factors of these alloys. An average coordination number of 10 (with about 5-7 Ca, 2-3 Mg and 1-2 Cu atoms) is most common for the Cu-centered clusters. The average coordination numbers around Mg and Ca are 12-13 ( $\sim 6$ -8 Ca, 3 Mg and 1-4 Cu) and 13-15 (7-9 Ca, 3-4 Mg, and 2-5 Cu), respectively, and they are composition dependent. Strong interaction of Cu with Mg and Ca, which result in pair bond shortening, has been identified. Icosahedral short range order does not dominate in these amorphous alloys, although polytetrahedral packing and five-fold bond configurations resulting in pentagonal bi-pyramids have been found to be the most common nearest atom configurations.

PACS numbers: 6143.Dq, 6105.fm, 6125.Mv, 6143.Bn, 83.10.Rs

## 1. INTRODUCTION

It is well established that Ca-Mg- based metallic glasses have very good glass forming ability (GFA) [1,2,3,4,5,6]. Based on two simple metal elements, these glasses have properties that distinguish them from transition-metal-based bulk metallic glasses (BMGs), such as very low Young's and shear moduli that are comparable with the moduli of human bones [7,8], very low density ( $1.6\text{-}2.8\text{ g/cm}^3$ ) [9], and strong relaxation dynamics of the super-cooled liquid [10]. Glass forming ability, as well as physical and mechanical properties of metallic glasses, is believed to depend on the type of short range order (SRO) and medium range order (MRO) of alloying elements in the amorphous structure. It is therefore interesting to know how the amorphous structure of Ca-Mg-based BMGs differ from transition-metal-based BMG structures.

Structural analysis of metal-metal BMGs has focused on transition metals glasses such as Zr-Cu [11,12,13,14], Zr-Pt [15], and Zr-Cu-Al [16,17]. The results indicate that the packing of atoms in these materials is not random, but is strongly influenced by chemical interactions. In particular, icosahedral SRO has been identified and its importance on relaxation dynamics, GFA and mechanical properties of these BMGs has been discussed. Transition metal - metalloid glasses such as Fe-C and Ni-B [18,19,20], which have marginal GFA, and many Al – transition metal glasses with high Al content [21], are not characterized by icosahedral SRO. These observations have been used to support a strong correlation between icosahedral SRO and good GFA [22].

In spite of good GFA, the atomic structure of  $\text{Ca}_{60}\text{Mg}_x\text{Zn}_{40-x}$  BMGs using X-ray and neutron diffraction and Reverse Monte Carlo (RMC) simulation [23] show no icosahedral SRO. The basic building blocks of the amorphous structure in these glasses are Mg- and Zn- centered clusters with primarily Ca atoms in the first coordination shell. The average coordination number (CN) around Zn is 9-10 [ $\sim 6\text{-}7\text{ Ca} + 3\text{ (Mg+Zn)}$ ], with dominant (0,3,6,0) and (0,2,8,0) polytetrahedral-type clusters, and the CN around Mg is 11-12 [ $\sim 7\text{-}8\text{ Ca} + 4\text{ (Mg+Zn)}$ ], with a large fraction of (0,2,8,1) and (0,2,8,2) clusters. Ca atoms have an average CN of 13. *Ab initio* simulations support these results. Although full icosahedra do not dominate in Ca-Mg-Zn BMGs, five-fold bonds in the form of pentagonal bi-pyramids are the most populous structural units and dominate in the clusters [23]. A large fraction of five-fold bonds and the lack of icosahedral SRO has also been found in the molecular dynamic (MD) simulated amorphous structure of Mg-Cu alloys [24]. The average CN around Cu and Mg is composition dependent, changing from less

than 10 with no icosahedral clustering to above 12 with increasing Cu content. Only on the Cu-rich side, where the CN is close to 12, does a predominance of five-fold bonds indicate Cu-centered icosahedral SRO, which is similar to the Zr-Cu case [11,12,13,14]. However, direct correlation between the icosahedral SRO and glass forming ability has not been established. The composition dependence of GFA in Ca-Mg-Cu glasses has been well established [5,6]. The GFA and relaxation dynamics of some of these alloys are similar or even slightly better than those of the best Ca-Mg-Zn BMGs [9,10]. At the same time, Ca-Mg-Cu BMGs have better corrosion resistance [25,26] and seem to be stronger than Ca-Mg-Zn BMGs [7,8,9]. In addition, strong covalent-like interactions between Cu-Mg and Cu-Ca have been noticed [5]. It is therefore useful to compare the amorphous structures of Ca-Mg-Cu and Ca-Mg-Zn BMGs. In the present work, the atomic structures of  $\text{Ca}_{40+X}\text{Mg}_{25}\text{Cu}_{35-X}$  BMGs are studied using a synergistic combination of neutron diffraction, quantum molecular dynamic (QMD) simulation and constrained reverse Monte Carlo (CRMC) simulation. These results are compared with an earlier analysis of the structure of Ca-Mg-Zn metallic glasses [26].

## 2. EXPERIMENTAL PROCEDURES

Fully amorphous samples of compositions,  $\text{Ca}_{40+X}\text{Mg}_{25}\text{Cu}_{35-X}$ , where  $X = 0, 5, 10$  and  $20$  at.%, were prepared by melt-spinning in the form of ribbons as described in [23]. The densities,  $\rho_0$ , of the amorphous alloys were measured with a helium pycnometer AccuPyc 1330 V1.03 and the values (in  $\text{g/cm}^3$  and  $\text{atoms/\AA}^3$ ) are given in Table 1. Neutron diffraction experiments were conducted at room temperature under vacuum using the General Materials (GEM) diffractometer at the ISIS high-intensity pulsed neutron source (Rutherford Appleton Laboratory, Didcot, UK) [27]. GEM has eight detector banks that collect data over a wide range in  $Q$  (from  $0.1$  to  $100 \text{ \AA}^{-1}$ ), where  $Q=4\pi \sin \Theta/\lambda$  is the magnitude of the scattering vector for a neutron of wavelength  $\lambda$  scattered at an angle  $2\Theta$ . Just prior to the neutron diffraction experiment, the ribbon samples were crushed into powder and loaded into  $10.3$  mm diameter cylindrical vanadium containers. The thickness of the container walls was  $25 \text{ }\mu\text{m}$ . Data reduction, correction and analysis were carried out using the program GUDRUN [28] and the ATLAS suite of programs [29]. This yielded the experimental total-scattering structure factors (SSF),  $S(Q)$ :

$$S(Q) = \sum_{i,j=1}^n c_i c_j b_i b_j [A_{ij}(Q) - 1] = \frac{1}{N} \frac{d\sigma}{d\Omega} - \sum_{i=1}^n c_i b_i^2 \quad (1)$$

Here  $\frac{1}{N} \frac{d\sigma}{d\Omega}$  is the differential neutron cross-section per unit solid angle  $\Omega$  for the  $n$ - component alloy ( $n = 3$  here),  $c_i$  and  $b_i$  are, respectively, the atomic fraction and the coherent bound neutron scattering length of element  $i$ ,  $A_{ij}(Q)$  are the Faber-Ziman partial structure factors [30], and  $4\pi \sum_{i=1}^n c_i b_i^2$  is the total-scattering cross section of the alloy. Each  $S(Q)$  was Fourier transformed to give a real space neutron total radial distribution function (RDF),  $G(r)$ , defined as [31]:

$$G(r) = \sum_{i,j=1}^n c_i c_j b_i b_j [g_{ij}(r) - 1] = \frac{1}{2\pi^2 r \rho_o} \int_0^\infty Q S(Q) L(Q) \sin(rQ) dQ \quad (2)$$

Here  $\rho_o$  is the average density of the alloy (in atoms per  $\text{\AA}^3$ ),  $r$  is a distance from an average origin atom in the amorphous structure, and  $g_{ij}(r)$  are the partial radial distribution functions (PRDF), which are defined as:

$$g_{ij}(r) = \frac{1}{4\pi r^2 c_j \rho_o} \frac{dn_{ij}(r)}{dr} \quad (3)$$

where  $dn_{ij}$  are the number of elements of type  $j$  between distances  $r$  and  $r+dr$  from an element of type  $i$ . The Lorch modification function [32],  $L(Q)$ , with a maximum momentum transfer  $Q_{\max}$  of  $25 \text{ \AA}^{-1}$  was used to reduce termination ripples in the Fourier transform (Equation 2). Combining equations (1) and (2) gives the following relation between  $g_{ij}(r)$  and  $A_{ij}(Q)$ :

$$2\pi^2 r \rho_o [g_{ij}(r) - 1] = \int_0^\infty Q [A_{ij}(Q) - 1] L(Q) \sin(rQ) dQ \quad (4)$$

Using Equation (3), the partial coordination number of an element  $j$  in the first coordination shell of the element  $i$  is determined:

$$N_{ij} = 4\pi c_j \rho_o \int_{r_{\min}}^{r_{\max}} g_{ij} r^2 dr \quad (5)$$

Here  $r_{\min}$  and  $r_{\max}$  are the positions of the start and end of the first peak in the respective  $g_{ij}(r)$ . QMD simulation of the Ca-Mg-Cu amorphous structures was conducted using the Vienna Ab-initio Simulation Package (VASP) [33]. The Projector Augmented-Wave (PAW) method [34,35] and Perdew-Burke-Ernzerhof (PBE) functional [36] were used to describe interacting valence electrons. Cubic simulation boxes with periodic boundary conditions contained 200 atoms, and the box size was determined by the density of the modeled material. The liquid was equilibrated at 1000K, then was quenched to 300K in 100K temperature steps, equilibrating at each

temperature for 3000 steps. Another 3000 consecutive configurations were further sampled at 300K with a time step of 5 fs, and an averaged PRDF was calculated from these configurations, thus taking into account thermal vibrations and assuming no structural relaxation within 15 ps.

The QMD model provided simulated PRDFs,  $g_{ij}^{\text{QMD}}(r)$ , for every studied alloy.

To expand the volume of the simulated structures and better fit to experimental diffraction data, alloy density and closest approach constraints, the CRMC simulation technique described in detail in [37] was used. Simulation boxes with periodic boundary conditions contained 1600 atoms, and the box volume was determined by the density of the material. The input data for the CRMC simulation were  $S(Q)$ ,  $G(r)$ , and  $g_{ij}^{\text{QMD}}(r)$ . Renormalization of  $g_{ij}^{\text{QMD}}(r)$  was allowed to correct possible QMD simulation errors. More than 10 million accepted random atom moves occurred for each sample during the CRMC simulation before the final configurations provided acceptable fits to the experimental data. This assured total independence of the modeled structures on the initial configurations of randomly distributed atoms.

The simulated structures were statistically analyzed using pair and three-body correlation functions, Voronoi tessellation and nearest neighbor approaches, which allowed calculation of local structural features such as total and partial CN, triplet angle correlations, type and distribution of characteristic coordination polyhedra, local packing fraction SRO and MRO.

### 3. RESULTS

#### 3.1 Neutron Diffraction Analysis

The experimental SSFs,  $S(Q)$ , for the four samples are shown in Figure 1a and the RDFs,  $G(r)$ , are shown in Figure 2a. The  $S(Q)$  curves damp very quickly with  $Q$  and no oscillations are apparent beyond  $\sim 15 \text{ \AA}^{-1}$ , indicating that the glasses have a wide range of interatomic distances. As the Cu concentration increases, the first sharp diffraction peak (FSDP) shifts to higher  $Q$  and broadens (Figure 1b). The RDFs show that an increase in Cu content shortens the average interatomic distance, and decreases the distribution width of the interatomic distances (Figure 2b). Thus the shift and broadening of the FSDP with an increase in the Cu content can be interpreted as arising from the shortening of the average interatomic distance and narrowing of the distribution of interatomic distances, respectively. There is also a pre-peak at  $Q \approx 1.2 \text{ \AA}^{-1}$  in the  $S(Q)$  curves, which indicates the presence of medium range order in these alloys [38,39].

Systematic changes of the shape of the first RDF peak with composition are observed (Figure 2a). In particular, the first RDF peak in  $\text{Ca}_{60}\text{Mg}_{25}\text{Cu}_{15}$  has two maxima, one at  $r = 3.11 \text{ \AA}$  and another, higher intensity, at  $r = 3.63 \text{ \AA}$ . As the amount of Cu increases, the relative intensity of the first maximum increases and its position slips to lower  $r$ -values (Figure 2b), while the second maximum degenerates into a small bump in alloys with 25 and 30% Cu and disappears in the alloy with 35% Cu. At the same time, an additional maximum starts to develop at  $r \approx 2.63 \text{ \AA}$ , preceding the first maximum, in the alloys with 30% and 35% Cu. Such a strong concentration dependence of the shape of the first RDF peak is apparently due to an increase in the fraction of shorter Cu-Cu and Cu-Mg bond pairs and a decrease in the fraction of longer Ca-Ca and Ca-Mg bond pairs with an increase in the amount of Cu.

### 3.2 Quantum Molecular Dynamic Simulation

Figure 3 shows the six QMD-simulated PRDFs for the  $\text{Ca}_{40}\text{Mg}_{25}\text{Cu}_{35}$ ,  $\text{Ca}_{50}\text{Mg}_{25}\text{Cu}_{25}$  and  $\text{Ca}_{60}\text{Mg}_{25}\text{Cu}_{15}$  alloys. The PRDFs are rather smooth since they account for atom vibrations. The effect of composition on the width and position of the first PRDF peak is weak relative to the effect on the positions and intensities of the higher order peaks. This indicates, to the first order, that bond distances between respective atom pairs in the first coordination shell are not affected by composition and that the partial coordination number of element  $j$  around element  $i$  is linearly proportional to the concentration  $c_j$  and alloy density  $\rho_o$  (see Equations 3 and 5). From the QMD-simulated PRDFs and using Equation (2), simulated total RDFs were obtained for every alloy and compared with the respective experimental neutron RDFs (Figure 4). A very good match is seen. Since QMD simulations were done completely independently from the neutron diffraction experiments, these good fits indicate that the simulated PRDFs are acceptable and reliable. The average partial and total coordination numbers around Ca, Mg and Cu atoms, from the QMD simulations, are given in Table 2 and the most frequent (mode,  $r_{ij}^{Mode}$ ), weighted average (mean,  $r_{ij}^{Mean}$ ) and cut-off (maximum,  $r_{ij}^{Cut-off}$ ) distances between atom pairs in the first coordination shell are given in Table 3, Table 4, and Table 5, respectively. The weighted average distances,  $r_{ij}^{Mean}$ , between the  $i$  and  $j$  atoms were calculated using the following equation [23]:

$$r_{ij}^{Mean} = \frac{\int_0^{r_{ij}^{Cut-off}} r_{ij} g_{ij}(r) dr}{\int_0^{r_{ij}^{Cut-off}} g_{ij}(r) dr} \quad (6)$$



### 3.3 Constrained Reverse Monte Carlo Simulation

The QMD-simulated PRDFs,  $g_{ij}^{\text{QMD}}(r)$ , were used as soft constraints in CRMC simulations to force the local atomic order to be consistent with experimental  $S(Q)$  and  $G(r)$  and simulated  $g_{ij}^{\text{QMD}}(r)$ . Renormalization of  $g_{ij}^{\text{QMD}}(r)$  during CRMC allowed minor adjustment of the QMD simulation to give much better fits of the CRMC-simulated  $S(Q)$  and  $G(r)$  to the experimental functions (Figure 5). The CRMC PRDFs are shown in Figure 6. Similar to QMD results, the first peak position almost does not depend on alloy composition, however, the peak intensity does. Using these PRDFs and Equation (3), the partial coordination numbers, as well as the mode, mean and maximum cut-off distances between the pair atoms in the first coordination shell, were calculated and the results are given in Table 2, Table 3, Table 4, and Table 5, respectively.

#### 3.3.2 Voronoi Analysis of Ca-Mg-Cu Amorphous Structure

Voronoi analysis was used to study local atom environments beyond the PRDFs results [23,40]. In Voronoi analysis, atoms that have common faces in their Voronoi polyhedra are nearest neighbors and a *coordination polyhedron* with vertices at the first-shell atom positions and edges coinciding with the interatomic bonds is defined for any chosen atom  $i$  [41]. Each coordination polyhedron, also called an  $i$ -centered cluster [40,42,43], is associated with the respective  $i$ -centered Voronoi polyhedron and can be assigned a Voronoi signature ( $\mathbf{v}_3, \mathbf{v}_4, \mathbf{v}_5, \mathbf{v}_6$ ). For Voronoi polyhedra,  $\mathbf{v}_m$  is the number of faces containing  $m$  edges; while for the respective coordination polyhedron,  $\mathbf{v}_m$  is the number of vertices common to  $m$  polyhedron edges (or faces) [44]. In the latter case,  $m$  is also called the vertex coordination. Those  $i$ -centered coordination polyhedra with the same Voronoi signature are considered to be topologically equivalent (even though they may not be identical) because they can be transformed into each other without changing the number of vertices and connecting edges. In addition to assigning topology, the Voronoi signature also defines the total coordination number ( $N_i$ ) of the  $i$ -centered cluster as  $N_i = \sum \mathbf{v}_m$ . Clusters with the same Voronoi signature can be chemically different. Therefore, in addition to the Voronoi signature, partial coordination numbers, i.e. the number of atoms of different species, should also be known for a more complete description of the SRO in the amorphous structure. The partial and total coordination numbers obtained with Voronoi tessellation of the CRMC-simulated

amorphous structure of  $\text{Ca}_{40+X}\text{Mg}_{25}\text{Cu}_{35-X}$  alloys are given in Table 2. They are in good agreement with those obtained with the use of the CRMC-simulated PRDFs.

Figure 7 illustrates the types and fractions of Ca-, Mg- and Cu- centered coordination polyhedra in the CRMC-simulated amorphous structures. Although many types of coordination polyhedra are present, the most common clusters are (0,2,8,4) for Ca-centered, (0,2,8,2) for Mg-centered, and (0,3,6,0) and (0,2,8,1) for Cu-centered clusters. The fractions and distributions of the clusters depend on alloy composition. Figure 8 shows the fractions of 3-, 4-, 5-, and 6- coordinated vertices in the Ca-, Mg- and Cu- centered clusters in the Ca-Mg-Cu amorphous alloys. The five-coordinated vertices dominate in all clusters, which is an indication that pentagonal bi-pyramids are the main building blocks in these amorphous alloys. Taking into account that the pentagonal bi-pyramid consists of five tetrahedra, one may conclude that polytetrahedral packing plays an important role in the formation of the amorphous structure in the Ca-Mg-Cu alloys.

Radical Voronoi tessellation gives the Voronoi cell volume (VCV) of each individual atom. The average VCV values of Ca, Mg and Cu atoms are given in Table 6. The VCV is higher for larger atoms. The VCV of Ca and Cu increases, while that of Mg is nearly constant or increases slightly, with decreasing Cu concentration. Assigning the effective atomic radius of element  $i$  as half the mode  $i$ - $i$  bond distance (Table 3), the average void volume and packing fraction near  $i$  atoms were calculated for each alloy as the difference between the respective Voronoi volume and the volume of atom  $i$ , and as the fraction of the atom volume relative the VCV, respectively (Table 6). The volume of voids and the packing fraction are higher near larger atoms. The void volume increases but the packing fraction decreases near Ca and Mg atoms with a decrease in Cu concentration. The packing fraction of Cu does not depend on the alloy composition within the 25-35% Cu range. However, it decreases in  $\text{Ca}_{60}\text{Mg}_{25}\text{Cu}_{15}$ . The average packing fraction of the alloys determined from their density (Table 6) shows similar trends and increases from 0.68 to 0.73 when the Cu content increases from 15% to 35%. These values show that packing is significantly more efficient than in monatomic, dense-random packed structures, and is comparable to packing efficiencies in crystalline metals.

### 3.3.3 Three-Body Correlations

Three-body correlations can provide additional information about the most common local structures around a centered atom because the characteristic angles between bonds connecting

any two atoms located in the first or second coordination shell with the centered atom are very sensitive to the spatial atom distribution [22]. Figure 9 illustrates the bond angle distributions in the  $\text{Ca}_{45}\text{Mg}_{25}\text{Cu}_{30}$  amorphous alloy within the first and second coordination shells. The upper limits of the bond lengths for the first shell were set to the cut-off values given in Table 5, while the bond length ranges for the second shell were set between the values corresponding to the first and second minima of the PRDFs (see Figure 6). Two characteristic maxima, one in the range of  $50\text{-}70^\circ$  and another between  $100\text{-}140^\circ$ , are clearly seen in the triplet distributions for the first coordination shell (Table 7). At least three maxima were identified in bond angle distributions for the second coordination shell. These are near  $30^\circ$ ,  $60^\circ$  and  $90^\circ$  (Table 8).

### 3. DISCUSSION

QMD simulated structures give smaller CNs for Cu-Cu, Cu-Mg, Mg-Mg and Mg-Cu and larger Ca-Ca, Ca-Mg, Ca-Cu, Mg-Ca and Cu-Ca CNs than does CRMC (Table 2). QMD simulated structures also give larger mean (Table 4) and cut-off (Table 5) pair atom distances. Given the very high QMD quench rate and the periodic boundary condition on a relatively small volume, these minor discrepancies in structural details are not surprising. At the same time, CNs obtained with Voronoi tessellation are in full agreement with CNs obtained directly from the CRMC partial RDF's. Thus, only the CRMC-simulated amorphous structures will be discussed here.

#### 3.1. Pair Bond Distance Correlations

$r_{\text{Mode}}$  values (Table 3) are always smaller than the respective  $r_{\text{Mean}}$  values (Table 4). The difference is smallest for Ca-Ca pairs (3.2%) and increases in the order of Ca-Mg (4.3%), Mg-Mg (7.7%), Ca-Cu (8.2%), Cu-Cu (8.8%), and Mg-Cu (13.5%). This indicates that the first-shell  $g_{ij}(r)$  peaks are asymmetric (non-Gaussian), especially for Cu- containing pairs.  $r_{\text{Mode}}$  and  $r_{\text{Mean}}$  values can be compared with atomic separations in crystalline metals and alloys. Crystalline metallic separations,  $r_M$ , and covalent distances,  $r_C$ , were estimated as a sum of metallic and covalent radii of respective elements (Table 9). The metallic radii are half the nearest distance between atoms in crystal lattices of the respective pure metals [69]. The covalent atomic separations [70] were obtained from analysis of nearest distances in crystalline intermetallic compounds using the Cambridge Structural Database. From Table 9, the  $r_{\text{Mean}}$  and  $r_{\text{Mode}}$  values for Ca-Ca atom pairs are smaller than  $r_M$ , so that the mean and mode Ca-Ca separations in Ca-

Mg-Cu glasses are slightly compressed. However, for all other atomic pairs  $r_{Mean}$  values are larger and  $r_{Mode}$  values are smaller than  $r_M$ . The larger mean separations suggest that some Mg and, especially, Cu atoms become slightly displaced from each other. It is likely that, similar to Zn in Ca-Mg-Zn amorphous alloys [23], some Cu atoms occupy gaps between the larger Ca and Mg atoms in the first coordination shell and their distances from the center atom vary depending on the gap sizes. At the same time,  $r_{Mode}$  for the atom pairs containing Cu are even smaller than the respective covalent bond distances in crystalline compounds, and the mode separations of Ca-Cu and Mg-Cu are well represented by the comparison between  $r_{Mode}$  and  $r_C$ . These data show that the absence of long-range order constraints allows shortening of first neighbor interatomic distances in amorphous structures, as compared to bond distances in crystalline metals and alloys.

The Mg-Cu (2.67 Å) and Ca-Cu (3.04 Å) mode pair distances and are much shorter than those calculated from the Ca-Ca, Mg-Mg and Cu-Cu  $r_{Mode}$  values (i.e. 2.81 Å and 3.13 Å, respectively, see Table 9). Shortening of Mg-Cu and Y-Cu bonds has been observed in amorphous  $Mg_{60}Cu_{30}Y_{10}$  [45]. Bond shortening has been discussed in amorphous and crystalline systems [46,47,48], and is likely related to *sp-d* electron hybridization [49]. This shortening is often associated with a covalent bonding component and indicates strong chemical interactions, suggesting that attractive forces will increase in the sequence: Ca-Mg, Ca-Cu and Mg-Cu. It has been suggested that the thermodynamic heat of mixing can represent this chemical interaction [50], and experimental data [51,52,53] give the heats of mixing of equimolar binary alloys as  $-6.0 \pm 1.0$  kJ/mol for Ca-Mg,  $-6.5 \pm 1.0$  kJ/mol for Ca-Cu and  $-9.0 \pm 1.0$  kJ/mol for Cu-Mg. These values give the same trend as for bond shortening, but the link between heats of mixing and bond lengths is phenomenological. Further, the heats of mixing give a global representation of interatomic bond enthalpies, which include the number of bonds formed and the energies of bonds between two atoms. Both of these values are likely to depend upon composition and local atom environment, so that trends in relative bond lengths obtained from heats of mixing should be used with caution.

The observation that nearest-neighbor bond lengths are shorter than those in the competing long-range ordered crystals may help explain why these are easy glass formers. The equilibrium crystalline phases that compete with the amorphous phase appear to minimize total energy by sacrificing optimal short-range order to achieve beneficial long-range order. On the other hand,

the absence of long-range atomic order allows metallic glasses to reduce the energy difference between the metastable glass and equilibrium crystal(s) by optimizing short-range atomic interactions and arranging the atoms in efficiently packed clusters [40,42,54,55]. The largest contribution to condensed phase stability is expected to come from nearest-neighbor interactions and volume minimization, so that the optimized short-range interactions, as well as the presence of MRO, in metallic glasses can produce structures that have only a small energetic disadvantage relative to the equilibrium crystalline structure [22,23]. Kinetic constraints from quenching restrict the long range atomic redistribution needed to achieve long-range order and to further minimize the total system energy, thus favoring glass formation. The present results suggest that metallic glasses not only have short range order, but may have “better” combination of short-range topological and chemical order (in terms of optimal bond length and/or atomic arrangement) than the competing crystals.

### 3.2 Coordination Numbers and Local Chemical Order

Increasing the Cu concentration from 15 to 35 at% continuously increases the total coordination number around Ca,  $CN_{Ca}$ , from 13.6 to 15.0 due to a faster increase in the number of smaller Cu atoms ( $CN_{Ca-Cu}$  increases from 1.7 to 4.4) and a slower decrease in the amount of the larger Ca atoms ( $CN_{Ca-Ca}$  decreases from 8.6 to 6.9) (Figure 11). On the other hand, the  $CN_{Mg}$  and  $CN_{Cu}$  almost do not depend on alloy composition. However, similar to the environment around Ca,  $CN_{Mg-Cu}$  and  $CN_{Cu-Cu}$  increase from 1.4 to 3.7 and from 0.6 to 2.6, respectively, while  $CN_{Mg-Ca}$  and  $CN_{Cu-Ca}$  decrease from 8.0 to 5.9 and from 6.8 to 5.0, respectively, with the increase in Cu concentration. The number of Mg atoms around Ca, Mg and Cu very weakly depends on alloy composition and, on average,  $CN_{Ca-Mg} = 3.5 \pm 0.2$ ,  $N_{Mg-Mg} = 2.8 \pm 0.3$  and  $CN_{Cu-Mg} = 2.7 \pm 0.3$  (see Table 2 and Figure 11), which may indicate a rather homogeneous Mg distribution. The dependences of the partial coordination numbers on Cu concentration can be described by linear equations (Table 10). Extrapolation to low Cu-concentrations predict no Cu-Cu first-neighbor interactions in alloys with Cu concentrations less than 10.3 at.%. At these low Cu concentrations,  $CN_{Cu-Ca}$  and  $CN_{Cu-Mg}$  are predicted to be 7.3 and 2.5, respectively,  $CN_{Ca} = 13$  and  $CN_{Mg} = 11.8$ . To determine the degree of chemical short range order (CSRO) around Ca, Mg and Cu atoms, the Warren-Cowley parameter,  $\alpha_{ij}$ , which is defined as [56]:

$$\alpha_{ij} = 1 - CN_{ij}/(c_j CN_i) \quad (7)$$

was used. Here  $c_j$  is the atomic fraction of the element  $j$ ,  $CN_{ij}$  is the partial coordination number of element  $j$  around the element  $i$ , and  $CN_i$  is the total coordination number around element  $i$ . A negative  $\alpha_{ij}$  ( $i \neq j$ ) indicates the presence of CSRO (i.e. the number of atoms  $j$  in the first shell exceeds the average concentration). For a random solution,  $\alpha_{ij}$  are zero. A modified CSRO parameter,  $\alpha_{i(jk)}$ , which is defined as

$$\alpha_{i(jk)} = 1 - (CN_{ij} + CN_{ik})/((c_j + c_k)CN_i) \text{ for } i \neq j \neq k \quad (8)$$

can also be used to analyze the CSRO in ternary alloys. Negative  $\alpha_{i(jk)}$  values indicate the presence of CSRO, while positive values indicate the presence of chemical short range clustering (CSRC) near the  $i$  atom.  $\alpha_{i(jk)}$  and  $\alpha_{ii}$  are dependent parameters, namely

$$(1 - c_i) \alpha_{i(jk)} = -c_i \alpha_{ii} \quad (9)$$

Therefore,  $\alpha_{ii} < 0$  should indicate CSRC (i.e. increased local concentration of like atoms) and  $\alpha_{ii} > 0$  should indicate CSRO around atom  $i$ .

Values of  $\alpha_{ij}$  and  $\alpha_{i(jk)}$  for Ca-Mg-Cu glasses are given in Table 11 and Table 12, respectively. The alloys show CSRC of Ca atoms that is largest for the alloy with 40% Ca ( $\alpha_{CaCa} = -0.16$ ) and it tends to decrease with an increase in Ca concentration (at 60% Ca  $\alpha_{CaCa} = -0.05$ ). Pronounced CSRO is detected near Cu atoms. These local regions are enriched with Ca and Mg, supporting the earlier observation of strong Ca-Cu and Mg-Cu bonding. Near Mg atoms,  $\alpha_{MgCa}$  is negative and  $\alpha_{MgCu}$  is positive, indicating enrichment in Ca and a Cu deficit in Mg-centered clusters. The  $\alpha_{i(jk)}$  criterion shows clear evidence of CSRC near Ca atoms and CSRO near Cu atoms when unlike elements are considered together (Table 12). At the same time,  $\alpha_{i(jk)}$  is almost zero or slightly negative for Mg-centered clusters indicating neutral environment.

### 3.3. Voronoi Tessellation Analysis

Voronoi analysis indicates that Kasper-type polyhedra dominate Ca-Mg-Cu glass structures. Among the clusters in Figure 7, (0,4,4,0), (0,3,6,0), (0,2,8,0), (0,2,8,1), (0,0,12,0), and (0,1,10,2) are non-distorted Kasper polyhedra, whereas (0,3,6,1), (0,4,4,2), (0,3,6,2), (0,4,4,3), (0,2,8,2), (0,3,6,3), (0,4,4,4), (0,2,8,3), (0,3,6,4), (0,4,4,5), (0,1,10,3), (0,2,8,4), (0,3,6,5), (0,4,4,6), (0,1,10,4), (0,2,8,5), (0,3,6,6), are distorted Kasper polyhedra with four-fold and six-fold disclinations [22], and only (0,3,7,4), (1,2,6,3), (1,2,5,2), (1,3,3,2) and (1,2,5,3) are other-type

polyhedra. The Kasper polyhedra edges can have different lengths— this is inevitable in glass; therefore, they are not identical even though they share the same topology (in terms of the Voronoi index) with the latter. Similar to other work [22], a cluster is identified here as a non-distorted Kasper polyhedron if it has a Voronoi index of the Kasper polyhedron and the term ‘distorted’ is assigned to Kasper polyhedra with disclinations.

Kasper polyhedra and their distorted variants account for over 50% of the nearest-neighbor clusters (Table 13). Since Kasper polyhedra are polytetrahedral, and many other polyhedra also contain tetrahedra, we conclude that the topological SRO of Ca-Mg-Cu is polytetrahedral in nature, which has been demonstrated in many other metallic glasses [22]. The current study therefore further supports the idea that the SRO of MGs is characterized by polytetrahedral packing via Kasper clusters and their distorted variants. The regularity of polytetrahedral packing can be evaluated using the ratio between the number of regular Kasper polyhedra and total number of regular and distorted Kasper polyhedra. We find that the atomic packing around smaller atoms (Cu) is much more regular polytetrahedral than around larger atoms (Ca). For example, the fractions of regular Kasper polyhedra around Cu is about 55%, around Mg range from 23% to 32% and decreases to 13-20% for Ca-centered clusters. This is reminiscent of Cu-Zr, where the packing around Cu appears much more regular than the packing around Zr [22]. The more regular packing around Cu can indicate that Cu-centered clusters are the primary structure-forming clusters, whereas Mg- and Ca-centered clusters are secondary clusters resulting from specific arrangements of atoms in the vertices of and voids between the Cu clusters (see section 3.5 below). This can also be explained by very strong interactions of Cu with Ca and Mg resulting in bond shortening. This feature could be quite general for metallic glasses, i.e., polytetrahedral packing is more prominent and better established around smaller atoms. This is probably because smaller atoms have smaller CNs, and thus have limited choices for efficient packing, in comparison to larger atoms with more neighbors and possibilities. Similar to Ca-Mg-Zn BMGs [23], the amorphous structures of Ca-Mg-Cu glasses contain a very low fraction of icosahedral SRO, in spite of the observation that five-coordinated vertices dominate in all clusters. A large fraction of five-fold bonds and the lack of icosahedral SRO have also been found in the MD-simulated amorphous structure of Mg-Cu alloys [24]. The dominance of five-fold vertices suggests that tetrahedra prefer to cluster into pentagonal bi-pyramids. Analysis of amorphous  $\text{Mg}_{60}\text{Cu}_{30}\text{Y}_{10}$  [Error! Bookmark not defined.] shows a prevalence of

fivefold bonds, with local atom arrangements very similar to the competing  $\text{Mg}_2\text{Cu}$  (Laves phase) and  $\text{YCu}_2$  crystals. Similar comparison of coordination polyhedra in the amorphous structure of  $\text{Ca}_{60}\text{Mg}_x\text{Zn}_{40-x}$  with polyhedra in the competing crystal phases,  $\text{CaMg}_2$  and  $\text{CaZn}$  [57], has shown that SRO arrangements around Ca and Mg atoms were different from those in the crystal phases [23]. However, the (0,3,6,0) Zn-centered coordination polyhedron, typical to  $\text{CaZn}$ , was one of the most common in the amorphous structure.

Amorphization of  $\text{Ca}_{60}\text{Mg}_{25}\text{Cu}_{15}$  competes with  $\text{CaMg}_2$  compound formation, amorphization of  $\text{Ca}_{40}\text{Mg}_{25}\text{Cu}_{35}$  competes with the  $\text{Cu}_2\text{Mg}$  phase, while solidification of  $\text{Ca}_{45}\text{Mg}_{25}\text{Cu}_{30}$  and  $\text{Ca}_{50}\text{Mg}_{25}\text{Cu}_{25}$  alloys forms three equally probable crystal phases,  $\text{CaMg}_2$ ,  $\text{Cu}_2\text{Mg}$  and  $\text{CaCu}$  [5,6].  $\text{CaMg}_2$  is a hexagonal Laves phase (space group  $\text{P6}_3/\text{mmc}$ , space group number 194) with lattice parameters  $a = 5.170 \text{ \AA}$  and  $c = 8.50 \text{ \AA}$ . This crystal structure contains three coordination polyhedra, two of which are Mg-centered (0,0,12,0) icosahedra with 6 Mg and 6 Ca atoms in the first shell, and the third is a Ca-centered (0,0,12,4) Friauf polyhedron containing 12 Mg and 4 Ca atoms in the first shell.  $\text{Cu}_2\text{Mg}$  is a cubic Laves phase (space group is  $\text{Fd-}3\text{m}$ , space group number 227) with the lattice parameter  $a = 6.990 \text{ \AA}$ . The crystal structure of this phase has two coordination polyhedra: a Cu-centered (0,0,12,0) icosahedron with 6 Cu and 6 Mg atoms in the first shell, and a Mg-centered (0,0,12,4) Friauf polyhedron with 12 Cu and 4 Mg atoms in the first shell. The  $\text{CaCu}$  phase has a primitive crystal structure (space group  $\text{P2}_1/\text{m}$ , space group number 11) with lattice parameters  $a = 19.47 \text{ \AA}$ ,  $b = 4.271 \text{ \AA}$ ,  $c = 5.880 \text{ \AA}$ , and  $\beta = 94.30^\circ$ . It has 10 characteristic coordination polyhedra, 5 of which are Cu-centered Kasper polyhedra (0,3,6,0) with 2 Cu and 7 Ca atoms in the first shell, and the other 5 are Ca-centered polyhedra (3,1,6,6,1), (6,1,2,2,4,0,2), (1,3,6,4,3), (3,3,3,4,3,0,1) and (1,3,7,6), with 7 Cu and 10 Ca atoms in the first shell. [58] (Additional indices in the Voronoi signatures of the Ca-centered polyhedra given above correspond to the number of 7-, 8-, and 9- coordinated vertices, respectively.)

None of the Ca-centered coordination polyhedra of the competing crystal phases are present in amorphous structures of Ca-Mg-Cu. The icosahedral SRO in the  $\text{CaMg}_2$  and  $\text{Cu}_2\text{Mg}$  crystal phases near Mg and Cu atoms, respectively, is not typical of Ca-Mg-Cu glass structures. The (0,3,6,0) Cu-centered coordination polyhedron in the  $\text{CaCu}$  phase is also common in the studied amorphous structures. This (0,3,6,0) Cu-centered cluster is probably the only link between the competing crystal and amorphous states and, therefore, a reduced fraction of this cluster in the amorphous structures should indicate better GFA. Indeed, the  $\text{Ca}_{60}\text{Mg}_{25}\text{Cu}_{15}$  and  $\text{Ca}_{40}\text{Mg}_{25}\text{Cu}_{35}$



amorphous alloys have much higher fraction of the (0,3,6,0) Cu-centered clusters than the better glass forming  $\text{Ca}_{45}\text{Mg}_{25}\text{Cu}_{30}$  and  $\text{Ca}_{50}\text{Mg}_{25}\text{Cu}_{25}$  alloys.

### 3.4. Three-Body Correlations

The Voronoi analysis above indicates that tetrahedra are dominant building blocks in amorphous structures of Ca-Mg-Cu alloys. With more than 50% frequency, the tetrahedra form pentagonal bipyramids and Kasper polyhedra. Because the characteristic vertex angles for regular tetrahedra are  $60^\circ$  and for the regular pentagonal bipyramids are  $60^\circ$  and  $108^\circ$ , the deviations of angle peak positions in three-body correlations indicate distortions from the regular configurations. These distortions are mainly caused by different radii of Ca, Mg and Cu atoms, as well as non-Gaussian distributions of the bond distances in the first coordination shell.

Table 7 gives the first and second maxima in bond angle distributions of Ca-Ca-Ca, Ca-Mg-Ca, Ca-Cu-Ca, Mg-Mg-Mg and Cu-Cu-Cu triplets in the first coordination shell. If like atoms are packed closely, then the characteristic angle for the *i-i-i* triplets will be equal or close to  $60^\circ$ . The first peak for Ca-Ca-Ca, Mg-Mg-Mg and Cu-Cu-Cu triplets occurs at  $\sim 57.9^\circ$ ,  $56.8^\circ$  and  $56.2^\circ$ , respectively. The peak shift to angles less than  $60^\circ$  indicates that the *i-i* distances within the first shell are longer than the bonds between the center and two first-shell *i* atoms. From Section 3.1, we take the distances between the center and shell like atoms as  $r_{Mode}$  and the distance between the shell atom pair as  $r_{Mean}$ , so that the angle of an *i-i-i* triplet is estimated as

$$\alpha = \cos^{-1}(r_{Mean}/2r_{Mode}) \quad (10)$$

The calculated angles for Ca-, Mg- and Cu-triplets using averaged  $r_{Mode}$  and  $r_{Mean}$  values from CRMC simulations (see Table 9) are  $58.9^\circ$ ,  $57.4^\circ$  and  $57.0^\circ$ , respectively. These are all within  $1^\circ$  of measured angles, giving good agreement.

For Ca-Mg-Ca and Ca-Cu-Ca triplets, the first peaks are at  $\sim 62.4^\circ$  and  $69.4^\circ$ , respectively. These larger angles result from the smaller atomic radii of Mg and Cu atoms. Using  $r_{Mode}$  for Ca-Ca, Ca-Mg and Ca-Cu separations, the Ca-Mg-Ca and Ca-Cu-Ca triplet angles are estimated as  $63.0^\circ$  and  $67.5^\circ$ , respectively. This is very good agreement for Ca-Mg-Ca, and shows reasonable agreement for Ca-Cu-Ca given the uncertainty in bond angles.

The second bond-angle distribution peak for Ca-Ca-Ca triplets is located near  $101^\circ$  in the  $\text{Ca}_{40}\text{Mg}_{25}\text{Cu}_{35}$  alloy and shifts to  $\sim 106^\circ$  in  $\text{Ca}_{60}\text{Mg}_{25}\text{Cu}_{15}$ . This is a little smaller than the  $108^\circ$  interior angle of a regular pentagon, and may be due to distortion when some vertices are

occupied by smaller Mg and Cu atoms. This also explains the angle decrease with increasing Cu concentration. Due to shorter Ca-Cu and Ca-Mg bonds, the interior angle at the Cu or Mg vertex increases at the expense of other interior angles, the sum of which is constant at  $540^\circ$ . Indeed, the second peak for Ca-Mg-Ca and Ca-Cu-Ca triplets is located at  $111-114^\circ$  and at  $121-130^\circ$ , respectively. Using these values of interior angles at Ca, Mg and Cu vertices, on average 2.6 Ca, 1.1 Mg and 1.3 Cu atoms in the  $\text{Ca}_{40}\text{Mg}_{25}\text{Cu}_{35}$  alloy and  $\sim 4.0$  Ca, 0.7 Mg and 0.3 Cu atoms in the  $\text{Ca}_{60}\text{Mg}_{25}\text{Cu}_{15}$  alloy are estimated per pentagon to satisfy the sum of vertex angles of  $540^\circ$ . The first three maxima in bond angle distributions of Ca-Ca-Ca, Ca-Mg-Ca, Ca-Cu-Ca, Mg-Mg-Mg and Cu-Cu-Cu triplets in the second coordination shell are given in Table 8 and Figure 9b. If like atoms contact in the second shell, then the characteristic first angle for  $i-i-i$  triplets will be equal or close to  $30^\circ$ . This angle is estimated for Ca-, Mg- and Cu triplets by assuming the  $i-i$  pair in the 2<sup>nd</sup> coordination shell are separated by  $r_{mode}$  and that the second shell is displaced from the central  $i$  atom by a distance  $(r_{mode} + \tilde{r})$ , where  $\tilde{r}$  is the weighted average of  $r_{mode}$  values for the atoms in the first shell of the  $i$  atom. The triplet angle is estimated as

$$\beta = \cos^{-1} \left\{ 1 - (1/2) \left[ r_{mode} / (r_{mode} + \tilde{r}) \right]^2 \right\} \quad (11)$$

The angles for a given  $i-i-i$  triplet are averaged over all four compositions. The estimated Ca-, Mg- and Cu triplet angles are  $30.8^\circ$ ,  $27.9^\circ$  and  $24.4^\circ$ , respectively, and are all within  $1^\circ$  of the measured angles ( $30.3^\circ$ ,  $27.3^\circ$  and  $24.5^\circ$ ). A similar topological analysis of Ca-Mg-Ca and Ca-Cu-Ca triplets for the 2<sup>nd</sup> coordination shell give estimated angles of  $32.2^\circ$  and  $34.0^\circ$ , which compare well with the measured values of  $31.5^\circ$  and  $32.8^\circ$ .

A second peak is expected near  $60^\circ$  when a full atom occurs between the  $i-i$  pair in the second shell, and the bond angle distributions show a rather broad peak centered very near  $60^\circ$  for the five triplets studied (Figure 9b). To model this, an atom with the effective radius of atoms in the 1<sup>st</sup> shell of  $i$  atoms is placed between the  $i-i$  atom pair in the 2<sup>nd</sup> shell so that,

$$\beta = \cos^{-1} \left\{ 1 - (1/2) \left[ (r_{mode} + \tilde{r}) / (r_{mode} + \tilde{r}) \right]^2 \right\} \quad (12)$$

By inspection, this gives an angle of  $60^\circ$  for each  $i-i-i$  triplet, in agreement with angles of  $61.0^\circ$ ,  $60.3^\circ$  and  $59.0^\circ$  from CRMC for Ca-, Mg- and Cu triplets. The Ca-Mg-Ca ( $61.1^\circ$ ) and Ca-Cu-Ca ( $61.6^\circ$ ) angles are both slightly larger than  $60^\circ$ . While this trend is matched using Equation 12 for these triplets, the estimated angles are somewhat larger ( $63.1^\circ$  and  $67.6^\circ$ , respectively).

A third peak in the second coordination shell may be expected near  $90^\circ$  by summing the 1<sup>st</sup> and 2<sup>nd</sup> peaks. While a local maxima is shown in all five bond angle distributions, it is a very shallow and broad distribution of angles. The many configurations for intervening atoms make it difficult to perform a simple topological analysis of the included angles.

### 3.5 Medium Range Order

The neutron diffraction pre-peak at  $Q \approx 1.2 \text{ \AA}^{-1}$  of Ca-Mg-Cu glasses (Figure 1) corresponds to certain medium-range correlations in real space [22]. Generally, MRO is seen in solute-lean glasses [15,59,60,61,62] and is explained in terms of a sublattice-like pattern formed by solutes [42] and significantly higher scattering amplitude for solute than for solvent atoms [22].

However, similar to this work, a pre-peak has also been seen in concentrated glasses, such as  $\text{Ce}_{55}\text{Al}_{45}$  [63] and  $\text{Ca}_{60}\text{Mg}_x\text{Zn}_{40-x}$  [23]. Our analysis, given below for the  $\text{Ca}_{45}\text{Mg}_{25}\text{Cu}_{30}$  metallic glass, shows that the MRO in Ca-Mg-Cu metal glasses is produced by a face center cubic (FCC) – like local ordering of Cu-centered clusters, and the pre-peak results from this FCC-like ordering combined with the strong neutron scattering from Cu.

Figure 12 shows six CRMC-simulated partial structure factors,  $A_{ij}(Q)$ , for the  $\text{Ca}_{45}\text{Mg}_{25}\text{Cu}_{30}$  metallic glass. The dashed vertical line in these figures corresponds to the position of the pre-peak maximum ( $Q = 1.25 \text{ \AA}^{-1}$ ) on the respective total  $S(Q)$  (see Figure 1a). It can be clearly seen that this pre-peak is originated from strong Cu-Cu and Mg-Cu correlations (Figure 12e and Figure 12f), as well as a weak Mg-Mg correlation (Figure 12d). No peak intensity is seen in this  $Q$  range for Ca-Ca, Ca-Mg and Ca-Cu correlations. This result indicates that, similar to solute-lean metallic glasses, MRO in Ca-Mg-Cu metal glasses is caused by solute-solute (mainly Cu-Cu and Mg-Cu) interactions.

Following a recent model [43], we assume that MRO is caused by local arrangement of Cu-centered clusters in an FCC motif, as shown schematically in Figure 13. This is supported not only by diffraction results, but also by the triplet angle distributions for the 2<sup>nd</sup> coordination shell, which show a surprising preference for angles of  $60^\circ$  and  $90^\circ$  irrespective of composition. An FCC cell consists of 4 Cu-centered clusters with 4 octahedral ( $\beta$ ) and 8 tetrahedral ( $\gamma$ ) interstitial sites, which tentatively can also be occupied by alloying elements. On average, each Cu-centered cluster consists of 11.4 atoms, so that the number of atoms per unit cell is estimated to be between 45.6 (no occupied interstitial sites) and 57.6 (all 12 sites are occupied). To satisfy

the alloy density ( $\rho_0 = 0.0373 \text{ \AA}^{-3}$ ) the cell volume,  $V_c$ , should therefore be between  $1223 \text{ \AA}^3$  and  $1544 \text{ \AA}^3$ , or the cluster unit cell parameter,  $a_c$ , should be between  $10.7 \text{ \AA}$  and  $11.6 \text{ \AA}$ . This results in the closest average distance between the Cu-centered clusters,  $r_{\text{Cu-Cu}}^{\text{Cluster}} (=a_c/\sqrt{2})$  to be between  $7.6 \text{ \AA}$  and  $8.2 \text{ \AA}$ . This distance corresponds to the third peak on the Cu-Cu PRDF, located at  $r = 7.8 \text{ \AA}$  (see Figure 6f). Assigning this value to  $r_{\text{Cu-Cu}}^{\text{Cluster}}$ , the parameter  $a_c$  is refined as  $a_c = 11.0 \text{ \AA}$ , which, at the given alloy density, gives 49.6 atoms per super-cell. This means that only 4 of the 12 interstitial sites (i.e.  $\sim 33\%$ ) per unit cell are occupied. Conducting similar analysis for the Mg-centered clusters gives the average distance between these clusters,  $r_{\text{Mg-Mg}}^{\text{Cluster}}$ , in the range of  $8.1 \text{ \AA}$  to  $8.6 \text{ \AA}$ . No peak is present on the Mg-Mg PRDF in this  $r$  range (see Figure 6d). We conclude that Mg-Mg clusters are not arranged in an FCC motif.

While the third peak on the Cu-Cu PRDF can be assigned to  $r_{\text{Cu-Cu}}^{\text{Cluster}}$ , which is the distance between the Cu-centered clusters in the  $\{0,0,0\}$  and  $\{1/2,1/2,0\}$  positions of the FCC super-cell, the wide second peak on the Cu-Cu PRDF can be assigned to the distances between the Cu in the center of the cluster and Cu located in the nearest tetrahedral and/or octahedral sites, as well as to the distance between nearest tetrahedral and octahedral sites. The small fourth Cu-Cu PRDF peak located at  $r = 9.2 \text{ \AA}$  can be assigned to the distance between a tetrahedral site and second nearest octahedral site or second nearest Cu-centered cluster. From crystallography, the center of a tetrahedral site in an FCC lattice is located at a distance  $r_{T1} = 0.433a_c$  of the nearest cell atom (Cu-centered cluster in our case) and  $r_{T2} = 0.83a_c$  of the second nearest cell atom, while the center of the octahedral site is located at the distance  $r_O = 0.5a_c$  of the nearest cell atom. The two characteristic distances between the octahedral and tetrahedral sites are  $r_{OT1} = 0.433a_c$  and  $r_{OT2} = 0.83a_c$ . Therefore, at  $a_c = 11.0 \text{ \AA}$ ,  $r_{T1} = r_{OT1} = 4.8 \text{ \AA}$  and  $r_O = 5.5 \text{ \AA}$  correspond to the second PRDF peak, and  $r_{T2} = r_{OT2} = 9.13 \text{ \AA}$  likely corresponds to the fourth Cu-Cu PRDF peak. Figure 14 shows good correlation between the Cu-Cu distances in the FCC super-lattice, formed of the Cu-centered clusters, and the peak maxima on the Cu-Cu partial radial distribution function. It can also be seen from this figure that the Cu-Cu MRO correlations are only present within one FCC super-cell and they disappear at distances higher than  $a_c$ .

The interstitial sites can tentatively be occupied not only by Cu but also Mg and/or Ca. Indeed, a detailed analysis, similar to the presented above, has led to a conclusion that the second peak in the Mg-Cu PRDF can be explained by the presence of Mg inside the tetrahedral and octahedral sites. However, the second peak in the Ca-Cu PRDF can be explained by the presence of Ca

inside octahedral sites only. There are no peaks in the Ca-Cu PRDF corresponding to the tetrahedral positions. This observation can be easily explained by a large size of Ca atoms, which would not fit the small tetrahedral sites [64].

### 3.6 Topological Description of Ca-Mg-Cu Atomic Structures

The present results give the most detailed experimental picture of a ternary metallic glass to date, and so it is worth analyzing the current findings with the efficient cluster packing (ECP) model for the atomic structure of metallic glasses [42,43,65]. In binary glasses, preferred radius ratios and strong chemical interactions between unlike atoms produce efficiently packed solute-centered clusters that are arranged in space with an FCC-like structure over a length scale of a few cluster diameters. In forming these clusters, solutes first tie up the other atoms in the structure, and higher solute concentrations give structures where the cluster-octahedral and cluster-tetrahedral interstices are progressively filled. At even higher solute concentrations, solutes replace solvent atoms in the cluster 1<sup>st</sup> shell. Structures where all of the cluster-interstitial sites and about 1/3 of the 1<sup>st</sup> shell are occupied by solvent atoms generally give the most stable binary glasses. A range of experimental and computational data supports this model.

It was earlier suggested that the largest solute in a multi-component glass would be the primary structure-forming solute, since larger solutes are topologically more potent [65]. However, the present work supports an earlier suggestion [19, 66] that elements with the strongest chemical interaction with solvent atoms will form the structure-forming clusters.

While much of the earlier analyses depend upon the nominal radius ratio between atoms, it has more recently been shown that the weighted average radius of atoms in the first coordination shell gives a good indication of GFA [67]. This effective radius ratio,  $\tilde{r}$ , correlates strongly with good GFA and gives an equivalent structural description regarding local partial coordination numbers [64]. This concept is used here to successfully model triplet angles. Although the nominal radius ratio for Cu and Ca is about 0.63 supporting a CN=8, the effective radius ratio is about 0.72. This suggests efficiently packed clusters with CN=9, which is less than the value of ~10 in the present work. The cut-off distance in the present work is about 30% longer than  $r_{mode}$  for Ca and Cu and 50% larger for Mg, which may contribute to this discrepancy.

The present data show different site filling rules for ternary glasses. Inter-cluster sites are essentially vacant in Ca-Mg-Cu glasses with Cu concentrations of 15% and 25% (Table 14), but

Cu-Cu contact occurs in all glasses (Table 2), suggesting that some Cu atoms occupy sites in the 1<sup>st</sup> coordination shell before inter-cluster sites are filled. Topological analysis suggests that sufficient Cu exists to begin filling some cluster-interstitial sites at 15% Cu, and the absence of this structural feature is consistent with the presence of Cu atoms in the 1<sup>st</sup> shell of Cu-centered clusters.

Solute-rich binary metallic glasses with solute atoms in the 1<sup>st</sup> coordination shell of solute-centered clusters are expected to have 4 cluster-interstitial atoms per structure-forming cluster [42,43,65], or 16 cluster-interstitial atoms per FCC unit cell. However, recent phenomenological analyses of multi-component BMGs show that they contain only 1 or 3 solute atoms, or ‘glue atoms’, per cluster [67,68]. In agreement with this, the present work shows 1 cluster-interstitial site per Cu-centered cluster in Ca<sub>45</sub>Mg<sub>25</sub>Cu<sub>30</sub> and 1.5 sites per cluster for Ca<sub>40</sub>Mg<sub>25</sub>Cu<sub>35</sub>.

With this as background, the present data gives the following topological picture of Ca-Mg-Cu structures. Cu-centered clusters in Ca<sub>60</sub>Mg<sub>25</sub>Cu<sub>15</sub> have a total CN of 9.8, so that the bulk concentration of Cu is achieved with 1.7 Cu atoms per cluster. There are no Cu atoms in cluster-interstitial sites (Table 14), so there is 1 Cu atom at the center of the cluster and 0.7 Cu atoms per cluster in the 1<sup>st</sup> coordination shell. This agrees very well with CN<sub>Cu-Cu</sub> of 0.6 (Table 2). The composition of Cu-centered clusters in Ca<sub>60</sub>Mg<sub>25</sub>Cu<sub>15</sub> is nearly equal to the bulk composition, further supporting this interpretation. The total CN around Cu clusters is 10.4 in Ca<sub>50</sub>Mg<sub>25</sub>Cu<sub>25</sub>, so there are 3.5 Cu atoms per structure-forming cluster. Data in Table 14 suggest there are no atoms in cluster-interstitial sites, so that there would be 1 Cu atom in the cluster center and 2.5 Cu atoms in the 1<sup>st</sup> coordination shell. However, this gives a partial CN that is larger than the value in Table 2, and the composition of Cu-centered clusters is noticeably deficient in Cu. Since the data in Table 14 has the largest uncertainty, this structural interpretation is unlikely. The bulk composition is achieved when 0.7 Cu atoms in cluster-interstitial sites are added to the Cu-centered cluster composition, so that an alternate interpretation is that there is 1 Cu atom at the center of the clusters, 0.7 Cu atoms in cluster-interstitial sites, and 1.8 Cu atoms in the 1<sup>st</sup> coordination shell of the Cu-centered clusters. This structure gives a partial CN<sub>Cu-Cu</sub> that is consistent with the data in Table 2 and with the observation of a peak in the Cu-Cu  $g(r)$  near 7.8 Å. The total Cu CN is 10.4 in Ca<sub>45</sub>Mg<sub>25</sub>Cu<sub>30</sub>, so there are 4.5 Cu atoms per cluster. The composition of Cu-centered clusters is deficient in Cu, so that an additional 0.7 Cu atoms per are needed to match the bulk composition. This suggests 1 Cu atom at the cluster center, 0.7 Cu

atoms at cluster-interstitial sites (Table 14), and 2.8 Cu atoms in the 1<sup>st</sup> coordination shell. This is consistent with the data in Table 14, with bulk composition and partial CNs, and with the Cu-Cu peak in  $g(r)$  near 7.8 Å. Finally, there are 5.5 Cu atoms per structure-forming cluster in  $\text{Ca}_{40}\text{Mg}_{25}\text{Cu}_{35}$ . To match bulk composition, 1.8 Cu atoms must occupy cluster-interstitial sites. Thus, there is 1 Cu atom at the cluster centers, 1.8 Cu atoms in cluster-interstitial sites, and 2.7 Cu atoms in the 1<sup>st</sup> coordination shell. This structure is consistent with the number of occupied interstitial sites from Table 14 ( $1.6 \pm 0.3$ ), with bulk composition and Cu-Cu partial CNs (Table 2), and with the Cu-Cu  $g(r)$ .

While bulk compositions can be matched by adding Cu atoms to cluster-interstitial sites, the Mg concentrations are still slightly deficient. The present work suggests that some Mg is in cluster-interstitial sites, consistent with this observation.

## CONCLUSIONS

1. The atomic structures of four  $\text{Ca}_{40+X}\text{Mg}_{25}\text{Cu}_{35-X}$  ( $X = 0, 5, 10, \text{ and } 20 \text{ at.}\%$ ) ternary metallic glasses have been determined using a synergistic combination of neutron diffraction, quantum molecular dynamics (QMD) and constrained reverse Monte Carlo (CRMC) modeling. All six partial radial distribution functions (PRDFs),  $g_{ij}(r)$ , have been identified for each alloy. The  $S(Q)$  curves damp very quickly with  $Q$  and no oscillations are apparent beyond  $\sim 15 \text{ Å}^{-1}$ , indicating that the glasses have a wide range of interatomic distances. An increase in Cu content shortens the average interatomic distance and narrows the distribution of interatomic distances, shifting the first sharp diffraction peak to higher  $Q$  and broadening the peak. A pre-peak at  $Q \approx 1.2 \text{ Å}^{-1}$  in the  $S(Q)$  curves indicates the presence of medium range order (MRO) in these amorphous alloys.
2. The first PRDF peaks, which correspond to interatomic bond distances in the 1st coordination shell, are asymmetric, and the mode bond distances are always smaller than the respective mean bond distances. The difference is the smallest for Ca-Ca pairs and increases in the order of Ca-Mg, Mg-Mg, Ca-Cu, Cu-Cu and Mg-Cu. This indicates that Ca-Ca atom pairs are most often compressed but often show ‘hard-sphere’ contact, and that Mg-Mg and Cu-Cu displacements most commonly show ‘hard-sphere’ contact but often have extended bond distances within the first shell. Atomic separations for unlike atom pairs are slightly shorter than the sum of atomic radii, suggesting that the atoms are slightly non-spherical.

3. The nearest-neighbor bond lengths are shorter than those in competing crystals. A noticeable shortening of Ca-Cu and Mg-Cu bond distances indicate strong interactions between these atom pairs. It is suggested that the bond shortening is enabled by the absence of long-range atomic order, which lowers the free energy of metallic glasses and increases GFA.
4. Pronounced chemical short range ordering (CSRO) near Cu atoms, chemical short range clustering (CSRC) near Ca atoms and a neutral environment near Mg atoms are shown. Increasing the Cu concentration from 15 to 35 atomic percent increases the total coordination number around Ca,  $CN_{Ca}$ , from 13.6 to 15.0, while  $CN_{Mg}$  and  $CN_{Cu}$  remain unchanged at those  $\approx 12.5$  and  $\approx 10.4$ , respectively. The partial coordination numbers depend nearly linearly on alloy composition, so that the number of Ca atoms decrease, the number of Cu atoms increase and the number of Mg atoms are almost constant with increasing Cu concentration.
5. Voronoi tessellation and three-body correlations show that many types of coordination polyhedra are present, but the most common are (0,2,8,4) Ca-centered, (0,2,8,2) Mg-centered and (0,3,6,0) and (0,2,8,1) Cu-centered. The fractions and distributions of these clusters depend on alloy composition. Polytetrahedral-type clusters and five-coordinated vertices dominate in the amorphous structures, which indicate that tetrahedra and pentagonal bi-pyramids are the main building blocks in these amorphous alloys. The GFA of the Ca-Mg-Cu alloys increases with a decreasing fraction of Cu-centered polytetrahedral clusters. The local atom packing fraction near a given atom increases with atomic radius and with an increase in Cu concentration. Global atom packing fractions of 0.68 to 0.73 are much larger than for dense random packed structures, and are comparable to packing in crystalline structures.
6. Medium range order is present in Ca-Mg-Cu amorphous alloys and is the result of strong tendency of Cu for CSRO. Detailed analysis shows that the amorphous structure of these alloys is described by close-packing of Cu-centered clusters that follows a face-centered cubic motif over a length scale of  $\sim 10$  Å, or about 3 cluster diameters. This gives a characteristic medium range order pre-peak at  $Q \sim 1.2$  Å<sup>-1</sup> in the total scattering structure factors of these alloys.
7. A topological description of Ca-Mg-Cu atomic structures shows that the effective radius of atoms in the 1<sup>st</sup> coordination shell of Cu atoms enables efficient atomic packing. These clusters match the bulk composition for Ca<sub>60</sub>Mg<sub>25</sub>Cu<sub>15</sub>, but are Cu-lean for all other compositions. The remaining structures have between 0.7 and 1.8 Cu atoms in cluster-interstitial sites. This allows the bulk composition to be matched and is necessary for agreement with the Cu-Cu  $g(r)$  plots.



Cu atoms occupy between 0.7 (for  $\text{Ca}_{60}\text{Mg}_{25}\text{Cu}_{15}$ ) and 2.8 (for  $\text{Ca}_{45}\text{Mg}_{25}\text{Cu}_{30}$ ) sites in the first coordination shells of Cu-centered clusters.

#### ACKNOWLEDGEMENTS

Extensive discussions with A. Hannon, A. Kolesnikov, and W. Dmowski and technical support from J.M. Scott and A. Hannon in conducting neutron experiments are recognized. The neutron experiments at the ISIS Pulsed Neutron and Muon Source were supported by a beamtime allocation (RB 820097) from the Science and Technology Facilities Council. Work at the Air Force Research Laboratory was supported through the Air Force Office of Scientific Research (M. Berman, Program Manager, Grant Number 10RX14COR) and the Air Force under on-site contract No. FA8650-10-D-5226 conducted through UES, Inc., Dayton, Ohio. Work at John Hopkins University was supported through the National Science Foundation under Contract No. NSF-DMR 0904188.

## TABLES

Table 1. Density (in  $\text{g/cm}^3$  and  $\text{atoms/\AA}^3$ ) of Ca-Mg-Cu amorphous alloys studied in this work.

Alloy	Density	
	$\text{g/cm}^3$	$\text{Atoms/\AA}^3$
$\text{Ca}_{40}\text{Mg}_{25}\text{Cu}_{35}$	$2.936 \pm 0.007$	0.03987
$\text{Ca}_{45}\text{Mg}_{25}\text{Cu}_{30}$	$2.673 \pm 0.005$	0.03728
$\text{Ca}_{50}\text{Mg}_{25}\text{Cu}_{25}$	$2.439 \pm 0.003$	0.03497
$\text{Ca}_{60}\text{Mg}_{25}\text{Cu}_{15}$	$2.039 \pm 0.003$	0.03097

Table 2. Partial and total coordination numbers around Ca, Mg and Cu atoms in the Ca-Mg-Cu amorphous alloys, in accord to QMD and RMC simulations and Voronoi (Vor) tessellation.

CN	$\text{Ca}_{40}\text{Mg}_{25}\text{Cu}_{35}$			$\text{Ca}_{45}\text{Mg}_{25}\text{Cu}_{30}$			$\text{Ca}_{50}\text{Mg}_{25}\text{Cu}_{25}$			$\text{Ca}_{60}\text{Mg}_{25}\text{Cu}_{15}$		
	QMD	CRMC	Vor	QMD	CRMC	Vor	QMD	CRMC	Vor	QMD	CRMC	Vor
Ca-Ca	7.0	6.9	7.0	7.8	7.1	7.1	8.6	7.9	7.9	9.2	8.6	8.6
Ca-Mg	4.3	3.7	3.6	4.1	3.7	3.8	3.8	3.4	3.4	3.5	3.3	3.4
Ca-Cu	4.9	4.4	4.4	3.9	3.8	3.8	3.2	3.1	3.1	1.6	1.7	1.7
Total	16.2	15.0	15.0	15.8	14.6	14.7	15.6	14.4	14.4	14.3	13.6	13.7
Mg-Ca	6.9	5.9	5.8	7.3	6.6	6.9	7.7	6.8	6.9	8.5	8.0	8.0
Mg-Mg	2.6	3.1	3.0	2.3	2.8	2.8	2.1	2.7	2.8	1.8	2.7	2.6
Mg-Cu	3.2	3.7	4.0	2.5	3.4	3.3	2.1	3.0	2.8	1.1	1.3	1.6
Total	12.8	12.7	12.8	12.2	12.8	13.0	11.8	12.5	12.5	11.3	12.0	12.2
Cu-Ca	5.6	5.0	5.1	5.9	5.6	5.7	6.4	6.2	6.2	6.4	6.8	6.7
Cu-Mg	2.3	2.7	2.9	2.1	2.8	2.7	2.1	3.0	3.0	1.8	2.4	2.6
Cu-Cu	1.6	2.6	2.1	1.3	1.9	2.0	1.0	1.2	1.5	0.6	0.6	0.8
Total	9.4	10.3	10.1	9.3	10.4	10.4	9.5	10.4	10.7	8.8	9.8	10.1

Table 3. The most frequent (mode) distances (in Angstroms) between pair atoms in Ca-Mg-Cu amorphous alloys, in accord to QMD and CRMC simulations.

Alloy	Method	Ca-Ca	Ca-Mg	Ca-Cu	Mg-Mg	Mg-Cu	Cu-Cu
Ca <sub>40</sub> Mg <sub>25</sub> Cu <sub>35</sub>	QMD	3.75	3.42	3.02	3.14	2.71	2.47
	CRMC	3.76	3.45	3.01	3.14	2.61	2.49
Ca <sub>45</sub> Mg <sub>25</sub> Cu <sub>30</sub>	QMD	3.75	3.41	3.03	3.13	2.71	2.48
	CRMC	3.74	3.43	3.04	3.12	2.62	2.49
Ca <sub>50</sub> Mg <sub>25</sub> Cu <sub>25</sub>	QMD	3.75	3.41	3.07	3.13	2.75	2.48
	CRMC	3.75	3.43	3.04	3.13	2.73	2.46
Ca <sub>60</sub> Mg <sub>25</sub> Cu <sub>15</sub>	QMD	3.78	3.46	3.03	3.08	2.72	2.51
	CRMC	3.78	3.47	3.08	3.12	2.70	2.50
Average	CRMC	3.76	3.45	3.04	3.12	2.67	2.49

Table 4. Weighted average (mean) distances (in Angstroms) between pair atoms in the first shell in Ca-Mg-Cu amorphous alloys, in accord to QMD and CRMC simulations.

Alloy		Ca-Ca	Ca-Mg	Ca-Cu	Mg-Mg	Mg-Cu	Cu-Cu
Ca <sub>40</sub> Mg <sub>25</sub> Cu <sub>35</sub>	QMD	3.95	3.64	3.21	3.31	2.83	2.59
	CRMC	3.89	3.55	3.19	3.34	3.03	2.85
Ca <sub>45</sub> Mg <sub>25</sub> Cu <sub>30</sub>	QMD	3.98	3.63	3.22	3.28	2.84	2.59
	CRMC	3.85	3.61	3.27	3.37	3.19	2.75
Ca <sub>50</sub> Mg <sub>25</sub> Cu <sub>25</sub>	QMD	4.01	3.62	3.25	3.24	2.89	2.58
	CRMC	3.89	3.59	3.33	3.30	3.15	2.63
Ca <sub>60</sub> Mg <sub>25</sub> Cu <sub>15</sub>	QMD	4.00	3.64	3.19	3.29	2.87	2.60
	CRMC	3.89	3.66	3.38	3.46	2.75	2.60
Average	CRMC	3.88	3.60	3.29	3.37	3.03	2.71

Table 5. The first shell cut-off distances between pair atoms (in Angstroms) in Ca-Mg-Cu amorphous alloys, in accord to QMD and CRMC simulations.

Alloy		Ca-Ca	Ca-Mg	Ca-Cu	Mg-Mg	Mg-Cu	Cu-Cu
Ca <sub>40</sub> Mg <sub>25</sub> Cu <sub>35</sub>	QMD	4.88	4.63	4.26	4.22	3.58	3.25
	CRMC	4.74	4.45	4.11	4.29	4.04	3.75
Ca <sub>45</sub> Mg <sub>25</sub> Cu <sub>30</sub>	QMD	4.91	4.59	4.26	4.09	3.58	3.34
	CRMC	4.73	4.63	4.31	4.26	4.34	3.54
Ca <sub>50</sub> Mg <sub>25</sub> Cu <sub>25</sub>	QMD	4.99	4.58	4.40	3.97	3.84	3.42
	CRMC	4.82	4.54	4.44	4.20	4.30	3.32
Ca <sub>60</sub> Mg <sub>25</sub> Cu <sub>15</sub>	QMD	4.94	4.58	4.13	4.05	3.89	3.31
	CRMC	4.84	4.70	4.41	4.46	3.92	3.22

Table 6. Voronoi cell volume, void volume and packing fraction of Ca, Mg, and Cu atoms in the amorphous structure of Ca-Mg-Cu alloys. The packing fractions of the alloys are also given in the last column.

	Voronoi Volume ( $\text{\AA}^3$ )			Void Volume ( $\text{\AA}^3$ )			Packing Fraction			
	Ca	Mg	Cu	Ca	Mg	Cu	Ca	Mg	Cu	Alloy
Ca <sub>40</sub> Mg <sub>25</sub> Cu <sub>35</sub>	35.99	24.12	13.50	8.16	6.64	5.42	0.78	0.73	0.61	0.73
Ca <sub>45</sub> Mg <sub>25</sub> Cu <sub>30</sub>	37.19	23.82	13.86	9.80	7.92	5.58	0.74	0.67	0.60	0.69
Ca <sub>50</sub> Mg <sub>25</sub> Cu <sub>25</sub>	38.71	24.45	13.16	10.65	9.30	5.27	0.73	0.63	0.61	0.69
Ca <sub>60</sub> Mg <sub>25</sub> Cu <sub>15</sub>	40.06	25.22	14.47	12.22	9.32	6.28	0.70	0.64	0.57	0.68

Table 7. Positions of the first and the second maxima (in degrees) in the bond angle distributions of five triplets within the first coordination shell in four Ca-Mg-Cu amorphous alloys.

1st shell	Ca-Ca-Ca	Ca-Mg-Ca	Ca-Cu-Ca	Mg-Mg-Mg	Cu-Cu-Cu
Ca <sub>40</sub> Mg <sub>25</sub> Cu <sub>35</sub>	57.0, 101.1	62.5, 111.1	71.7, 122.6	57.4, 108.2	52.8, 110.5
Ca <sub>45</sub> Mg <sub>25</sub> Cu <sub>30</sub>	58.0, 103.8	62.3, 111.1	69.6, 121.4	57.4, 110.4	55.4, 111.0
Ca <sub>50</sub> Mg <sub>25</sub> Cu <sub>25</sub>	58.2, 104.3	62.5, 113.1	69.8, 122.3	57.2, 108.5	55.5, 110.5
Ca <sub>60</sub> Mg <sub>25</sub> Cu <sub>15</sub>	58.4, 105.5	62.3, 113.3	66.5, 121.6	55.1, 108.9	61.2, 107.9

Table 8. Positions of three maxima (in degrees) observed in the bond angle distributions of five triplets within the second coordination shell in four Ca-Mg-Cu amorphous alloys.

2nd shell	Ca-Ca-Ca	Ca-Mg-Ca	Ca-Cu-Ca	Mg-Mg-Mg	Cu-Cu-Cu
Ca <sub>40</sub> Mg <sub>25</sub> Cu <sub>35</sub>	29.5, 62.5, 88.5	31.5, 63.0, 88.5	33.5, 61.5, 86.5	27.5, 63.5, 86.5	24.5, 60.0, 90.0
Ca <sub>45</sub> Mg <sub>25</sub> Cu <sub>30</sub>	30.5, 61.0, 85.0	31.5, 60.0, 92.5	33.5, 60.0, 90.0	27.5, 60.0, 90.0	25.5, 57.5, 90.0
Ca <sub>50</sub> Mg <sub>25</sub> Cu <sub>25</sub>	30.5, 60.0, 86.5	31.5, 60.0, 93.5	32.5, 62.5, 87.5	27.5, 60.0, 90.5	23.5, 60.0, 84.5
Ca <sub>60</sub> Mg <sub>25</sub> Cu <sub>15</sub>	30.5, 60.5, 84.5	31.5, 61.5, 90.0	31.5, 62.5, 94.5	26.5, 57.5, 85.0	24.5, 58.5, 95.5

Table 9. Metallic,  $r_m$ , [69] and covalent,  $r_c$ , [70] crystalline bond distances between Ca, Mg and Cu atom pairs. These distances are compared to  $r_{Mode}$  and  $r_{Mean}$  from the CRMC PRDFs.  $r_{Mode}$  and  $r_{Mean}$  are the average values for the four studied alloys.

	Ca-Ca	Ca-Mg	Ca-Cu	Mg-Mg	Mg-Cu	Cu-Cu
$r_M$ (Å)	3.94	3.57	3.25	3.20	2.88	2.56
$r_C$ (Å)	3.52	3.17	3.08	2.82	2.73	2.64
$r_{Mode}$ (Å)	3.76	3.45	3.04	3.13	2.67	2.49
$r_{Mean}$ (Å)	3.88	3.60	3.29	3.37	3.03	2.71
100%( $r_{Mean}/r_{Mode}-1$ )	3.2	4.3	8.2	7.7	13.5	8.8
100%( $r_M/r_{Mode}-1$ )	4.8	3.5	6.9	2.2	7.9	2.8
100%( $r_C/r_{Mode}-1$ )	-6.4	-8.1	1.3	-9.9	2.2	6.0
100%( $r_M/r_{Mean}-1$ )	1.5	-0.8	-1.2	-5.0	-5.0	-5.5

Table 10. Linear fits to the dependence on Cu content (at.%) of coordination number data (Figure 11).  $R^2$  is the coefficient of determination of the respective linear regression.

Atomic pair	Gradient	Intercept	$R^2$
Ca-Ca	-0.090	9.98	0.963
Ca-Mg	0.022	2.95	0.884
Ca-Cu	0.125	0.00	0.992
Mg-Ca	-0.101	9.48	0.978
Mg-Mg	0.018	2.36	0.639
Mg-Cu	0.110	0.00	0.956
Cu-Ca	-0.089	8.24	0.966
Cu-Mg	0.0154	2.32	0.278
Cu-Cu	0.099	-1.02	0.951

Table 11. Short-range order parameters,  $\alpha_{ij}$ , for Ca-, Mg- and Cu- centered clusters in the Ca-Mg-Cu amorphous alloys.

$\alpha_{ij}$	Ca-Ca	Ca-Mg	Ca-Cu	Mg-Ca	Mg-Mg	Mg-Cu	Cu-Ca	Cu-Mg	Cu-Cu
Ca <sub>40</sub> Mg <sub>25</sub> Cu <sub>35</sub>	-0.16	0.03	0.16	-0.15	0.00	0.17	-0.21	-0.05	0.28
Ca <sub>45</sub> Mg <sub>25</sub> Cu <sub>30</sub>	-0.07	-0.04	0.15	-0.17	0.15	0.14	-0.21	-0.08	0.38
Ca <sub>50</sub> Mg <sub>25</sub> Cu <sub>25</sub>	-0.10	0.05	0.14	-0.09	0.14	0.05	-0.15	-0.12	0.42
Ca <sub>60</sub> Mg <sub>25</sub> Cu <sub>15</sub>	-0.05	0.02	0.17	-0.11	0.11	0.25	-0.17	0.07	0.56

Table 12. The short-range order parameters,  $\alpha_{i(jk)}$ , for Ca-, Mg- and Cu- centered clusters in the Ca-Mg-Cu amorphous alloys.

$\alpha_{i(jk)}, i =$	Ca	Mg	Cu
Ca <sub>40</sub> Mg <sub>25</sub> Cu <sub>35</sub>	0.11	0.00	-0.15
Ca <sub>45</sub> Mg <sub>25</sub> Cu <sub>30</sub>	0.06	-0.05	-0.16
Ca <sub>50</sub> Mg <sub>25</sub> Cu <sub>25</sub>	0.10	-0.05	-0.14
Ca <sub>60</sub> Mg <sub>25</sub> Cu <sub>15</sub>	0.08	-0.04	-0.10

Table 13. Fractions of Ca-, Mg- and Cu-centered Kasper polyhedra, distorted Kasper polyhedra and sum of both.

	Kasper Polyhedra			Distorted Kasper Polyhedra			Sum		
	Ca	Mg	Cu	Ca	Mg	Cu	Ca	Mg	Cu
$\text{Ca}_{40}\text{Mg}_{25}\text{Cu}_{35}$	0.059	0.142	0.323	0.408	0.467	0.275	0.467	0.610	0.598
$\text{Ca}_{45}\text{Mg}_{25}\text{Cu}_{30}$	0.079	0.152	0.323	0.424	0.402	0.269	0.503	0.555	0.592
$\text{Ca}_{50}\text{Mg}_{25}\text{Cu}_{25}$	0.102	0.192	0.308	0.454	0.425	0.260	0.556	0.617	0.568
$\text{Ca}_{60}\text{Mg}_{25}\text{Cu}_{15}$	0.121	0.190	0.338	0.498	0.407	0.283	0.619	0.597	0.621

Table 14. The lattice parameter,  $a_c$ , the number of atoms per unit cell,  $N_c$ , and the number of occupied interstitial sites per unit cell,  $N_i$  in the face centered cubic lattice formed of the Cu-centered clusters in Ca-Mg-Cu amorphous alloys.

Alloy	$\text{Ca}_{40}\text{Mg}_{25}\text{Cu}_{35}$	$\text{Ca}_{45}\text{Mg}_{25}\text{Cu}_{30}$	$\text{Ca}_{50}\text{Mg}_{25}\text{Cu}_{25}$	$\text{Ca}_{60}\text{Mg}_{25}\text{Cu}_{15}$
$a_c$ (Å)	$10.9 \pm 0.1$	$11.0 \pm 0.1$	$10.9 \pm 0.1$	$11.2 \pm 0.2$
$N_c$	$51.6 \pm 1.5$	$49.6 \pm 1.5$	$45.3 \pm 1.3$	$43.6 \pm 2.3$
$N_i$	$6.4 \pm 1.5$	$4.0 \pm 1.5$	$0.0 \pm 1.3$	$1.2 \pm 2.3$

## FIGURE CAPTIONS

Figure 1. (a) Experimental total neutron scattering structure factors for  $\text{Ca}_{60-X}\text{Mg}_{25}\text{Cu}_{15+X}$  metallic glasses. The curves are separated by shifting along the vertical axis for better view. (b) Dependence on the concentration of copper of the positions of the start (1<sup>st</sup> Minimum), maximum (Peak) and end (2<sup>nd</sup> minimum) of the first peak, as well as the peak width.

Figure 2. (a) Total radial distribution functions for  $\text{Ca}_{60-X}\text{Mg}_{25}\text{Cu}_{15+X}$  metallic glasses. The curves are separated by shifting along the vertical axis for better view. (b) Dependence on the concentration of copper of the positions of the first, second and third peaks and the width of the first and second peaks.

Figure 3. QMD-simulated (a) Cu-Cu, (b) Mg-Cu, (c) Mg-Mg, (d) Ca-Cu, (e) Ca-Mg and (f) Ca-Ca PRDFs for  $\text{Ca}_{40}\text{Mg}_{25}\text{Cu}_{35}$ ,  $\text{Ca}_{50}\text{Mg}_{25}\text{Cu}_{25}$  and  $\text{Ca}_{60}\text{Mg}_{25}\text{Cu}_{15}$  metallic glasses.

Figure 4. Experimental (dark solid lines) and QMD-simulated (red dashed lines) RDFs for  $\text{Ca}_{60-X}\text{Mg}_{25}\text{Cu}_{15+X}$  metallic glasses. The curves are separated by 0.3-point shifting along the vertical axis for better view.

Figure 5. Experimental (dark solid lines) and CRMC-simulated (red dashed lines) (a) total structure factors and (b) RDFs for  $\text{Ca}_{60-X}\text{Mg}_{25}\text{Cu}_{15+X}$  metallic glasses. The curves are separated by shifting along the vertical axis for better view.

Figure 6. CRMC-simulated (a) Ca-Ca, (b) Ca-Mg, (c) Ca-Cu, (d) Mg-Mg, (e) Mg-Cu and (f) Cu-Cu partial radial distribution functions,  $g_{ij}(r)$  for  $\text{Ca}_{60-X}\text{Mg}_{25}\text{Cu}_{15+X}$  metallic glasses.

Figure 7. Distribution of different types of (a) Ca-centered (b) Mg-centered and (c) Cu-centered clusters in  $\text{Ca}_{60-X}\text{Mg}_{25}\text{Cu}_{15+X}$  amorphous alloys.

Figure 8. Fractions of 3-, 4-, 5- and 6- coordinated vertices in Ca-, Mg- and Cu- centered clusters in (a)  $\text{Ca}_{40}\text{Mg}_{25}\text{Cu}_{35}$ , (b)  $\text{Ca}_{45}\text{Mg}_{25}\text{Cu}_{30}$ , (c)  $\text{Ca}_{50}\text{Mg}_{25}\text{Cu}_{25}$ , and (d)  $\text{Ca}_{60}\text{Mg}_{25}\text{Cu}_{15}$  amorphous alloys.

Figure 9. Ca-Ca-Ca, Ca-Mg-Ca, Ca-Cu-Ca, Mg-Mg-Mg and Cu-Cu-Cu bond angle distributions in (a) the first coordination shell and (b) second coordination shell in the  $\text{Ca}_{45}\text{Mg}_{25}\text{Cu}_{30}$  amorphous alloy.



Figure 10. Comparison of the mode atomic pair distances with (a) the respective mean distances in the amorphous structure of the studied Ca-Mg-Cu alloys, and with the reported (b) metallic,  $r_M$ , and (c) covalent,  $r_C$ , bond distances.

Figure 11. Dependence on the Cu concentration of (a) the total coordination number,  $N_M$ , where M is Ca, Mg, or Cu center atom, and partial coordination numbers (b)  $N_{M-Ca}$ , (c)  $N_{M-Mg}$ , and (d)  $N_{M-Cu}$ .

Figure 12. Partial structure factors,  $A_{ij}(Q)$ , for  $Ca_{45}Mg_{25}Cu_{30}$  metallic glass.

Figure 13. Schematic of a face centered cubic cell formed by Cu-centered clusters (shown by red). Positions of octahedral ( $\beta$ ) and tetrahedral ( $\gamma$ ) interstitial voids are also shown.

Figure 14. Correlation of the Cu-Cu distances in the FCC super-lattice formed of the Cu-centered clusters and the intensity peaks on the Cu-Cu partial radial distribution function.

## REFERENCES

- 1 O.N. Senkov, J.M. Scott, Scripta Mater. 50 (2004) 449-452.
- 2 O.N. Senkov, J.M. Scott, Mater. Letters, 58 (2004) 1375–1378.
- 3 O.N. Senkov, J.M. Scott, J. Non-Cryst. Solids, 351 (2005) 3087-3094.
- 4 O.N. Senkov, J.M. Scott, D.B. Miracle, Materials Trans. 48 (2007) 1610-1616.
- 5 O.N. Senkov, J.M. Scott, D.B. Miracle, J. Alloys Comp. 424 (2006) 394-399.
- 6 O.N. Senkov, D.B. Miracle, J.M. Scott, Intermetallics 14 (2006) 1055-1060.
7. V. Keppens, Z. Zhang, O.N. Senkov, D.B. Miracle, Phil. Mag. 87 (2007) 503-508; V. Keppens, Z. Zhang, O.N. Senkov, D.B. Miracle, Mater. Sci. Eng. 87 (2007) 503-508.
- 8 Z. Zhang, V. Keppens, O.N. Senkov, D.B. Miracle, Mater. Sci. Eng. A 471 (2007), 151–154.
- 9 O.N. Senkov, D.B. Miracle, V. Keppens, P.K. Liaw: Metall. Mater. Trans. A 39A (2008) 1888-1900.
- 10 O.N. Senkov, D.B. Miracle, Metall. Mater. Trans. A 41A (2010) 1677-1684.
- 11 N. Mattern, A. Schöps, U. Kühn, J. Acker, O. Khvostikova, J. Eckert J. Non-Cryst. Solids 354 (2008) 1054–1060.
- 12 D. Ma, A.D. Stoica, X.L. Wang, Z.P. Lu, M. Xu, and M. Kramer, Phys. Rev. B 80 (2009) 014202.

- 13 Y.Q. Cheng, H.W. Sheng, E. Ma, *Phys. Rev. B* 78 (2008) 014207.
- 14 Y.Q. Cheng, A.J. Cao, H.W. Sheng, E. Ma, *Acta Mater* 56 (2008) 5263–5275.
- 15 N.A. Mauro, V. Wessels, J.C. Bendert, S. Klein, A.K. Gangopadhyay, M.J. Kramer, S.G. Hao, G.E. Rustan, A. Kreyssig, A.I. Goldman, K.F. Kelton, *Phys. Rev. B* 83 (2011) 184109.
- 16 Y.Q. Cheng, E. Ma, H.W. Sheng, *Phys. Rev. Lett.* 102 (2009) 245501.
- 17 K. Georgarakis, A.R. Yavari, D.V. Louzguine-Luzgin, J. Antonowicz, M. Stoica, Y. Li, M. Satta, A. LeMoulec, G. Vaughan, and A. Inoue *Appl. Phys. Lett.* 94 (2009) 191912.
- 18 P. Lamparter, W. Sperl, S. Steeb, *Z. Naturforsch* 37a (1982) 1223-
19. V.Yu. Kazimirov, D. Louca, M. Widom, X.J. Gu, S.J. Poon, G.J. Shiflet, *Phys Rev, B* 78 (2008) 054112.
20. H.W. Sheng, W.K. Luo, F.M. Alamgir, J.M. Bai, E. Ma, *Nature* 439(7075) (2006) 419-425.
- 21 H.W. Sheng, Y.Q. Cheng, P.L. Lee, S.D. Shastri, E. Ma, *Acta Mater.* 56 (2008) 6264-6272.
- 22 Y.Q. Cheng, E. Ma, *Progr. Mater. Sci.* 56 (2011) 379-473.
- 23 O.N. Senkov, D.B. Miracle, E.R. Barney, A.C. Hannon, Y.Q. Cheng and E. Ma, *Phys. Rev. B* 82 (2010) 104206.
- 24 N.P. Bailey, J. Schiotz, K.W. Jacobsen, *Phys. Rev. B* 69 (2004) 144205.
- 25 B.R. Barnard, P.K. Liaw, R.A. Buchanan, O.N. Senkov, D.B. Miracle, *Mater. Trans.*, 48 (2007) 1870-1878.
- 26 J. Dahlman O.N. Senkov J.M. Scott, D.B. Miracle, *Mater. Trans.*, 48 (2007) 1850-1854.
27. A. C. Hannon, *Nucl. Instrum. Methods in Phys. Research A* 551 (2005) 88-107.
28. A.K. Soper, Gudrun software, <http://www.isis.stfc.ac.uk/instruments/sandals/data-analysis/gudrun8864.html>.
29. A.C. Hannon, W.S. Howells, A.K. Soper, in: *Neutron Scattering Data Analysis*, *Inst. Phys. Conf. Ser.*, 107 (1990) 193-211.
- 30 T.E. Faber and J.M. Ziman, *Philos. Mag.* 11 (1965) 153-173.
- 31 D.A. Keen, *J. Appl. Cryst.* 34 (2001) 172-177.
- 32 E. Lorch, *J. Phys. C* 2 (1969) 229.
- 33 G. Kresse and J. Hafner, *Phys. Rev. B* 47 (1993) 558-561.
- 34 P.E. Blochl, *Phys. Rev. B* 50 (1994) 17953-17977.
- 35 G. Kresse and D. Joubert, *Phys. Rev. B*, 59 (1999) 1758-1775
- 36 J. P. Perdew, K. Burke, and M. Ernzerhof, *Phys. Rev. Lett.* 77 (1996) 3865-3869; *Phys. Rev. Lett.* 78 (1997) 1396.
- 37 R.L. McGreevy, *J. Phys.: Cond. Matter.* 13 (2001) R877-R913.
- 38 L. Zhang, Y.Wu, X.Bian, H.Li, W. Wang, S. Wu, *J. Non-Cryst. Sol.* 262 (2000) 169-176.
- 39 N.A. Mauro, V. Wessels, J.C. Bendert, S. Klein, A.K. Gangopadhyay, M.J. Kramer, S.G. Hao, G.E. Rustan, A. Kreyssig, A.I. Goldman, K.F. Kelton, *Phys. Rev. B* 83 (2011) 184109/1-8.
- 40 R. Zallen, *The Physics of Amorphous Solids*, Wiley-VCH, Weinheim, 2004.
- 41 F.C. Frank, J.S. Kasper, *Acta Crystallogr.* 11 (1958) 184-190.
42. D.B. Miracle, *Nature Mater.*, 3 (2004) 697-702; *Acta Mater.*, 54 (2006) 4317-4336.
- 43 D.B. Miracle, *Acta Mater.*, 54 (2006) 4317-4336.
- 44 J.L. Finney, *Proc. Roy. Soc. A* 319(1970) 495-507.
- 45 P. Jovari, K. Saksl, N. Pryds, B. Lebech, N. P. Bailey, A. Mellergård, R. G. Delaplane, and H. Franz, *Phys. Rev. B* 76 (2007) 054208.
- 46 D.B. Miracle, *Acta Metall. Mater.* 41 (1993) 649-684.
- 47 T. Egami, *J. Non-Cryst. Solids* 205-207 (1996) 575-582.

- 48 D.B. Miracle, O.N. Senkov, J. Non-Cryst. Solids 319 (2003) 174-191.
- 49 H. Jahn, E. Teller, Proc. Royal Soc. London, Ser. A: Math. Phys. Sci. 161 (905) (1937) 220-235.
- 50 A Takeuchi, A. Inoue; Mater. Trans. JIM, 46 (2005) 2817-2829.
- 51 S.P. Garg, Y.J. Bhatt, and C.V. Sundaram; *Metall. Trans.*, 4 (1973) 283-289.
- 52 F. Sommer, H.-G. Krull, J.J. Lee, J. Less-Common Metals 169 (1991) 361-368.
- 53 M. Hino, T. Nagasaka, R. Takehama, Metall. Mater. Trans. B 31B (2000) 927-935.
- 54 D.B. Miracle, W.S. Sanders, O.N. Senkov, Philos. Mag. 83 (2004) 2409.
- 55 D.B. Miracle, O.N. Senkov, W.S. Sanders, K.L. Kendig, Mater. Sci. Eng. A 3750377 (2004) 150-156.
- 56 B.E. Warren, X-ray Diffraction, Dover Publ., NY, 1990.
- 57 S. Gorsse, G. Orveillon, O.N. Senkov, D.B. Miracle, Phys. Rev. B 73 (2006) 224202.
- 58 J.L.C. Daams, P. Villars & J.H.N. van Vucht, Atlas of Crystal Structure Types for Intermetallic Phases. ASM International: 1991.
- 59 H.Y. Hsieh, T. Egami, Y. He, S.J. Poon, G.J. Shiflet, J. Non-Cryst. Solids 135 (1991) 248-254.
- 60 K. Saksl, P. Jovari, H. Franz, J.Z. Jiang, J. Appl. Phys 97 (2005) 113507/1-8.
- 61 K. Ahn, D. Louca, S.J. Poon, G.J. Shiflet, Phys. Rev. B 70 (2004) 224103.
- 62 S.Y. Wang, C.Z. Wang, M.Z. Li, L. Huang, R.T. Ott, M.J. Kramer, D.J. Sordellet, K.M. Ho, Phys. Rev. B 78 (2008) 184204.
- 63 H.W. Sheng, H.Z. Liu, Y.Q. Cheng, J. Wen, P.L. Lee, W.K. Luo, S.D. Shastri, E. Ma, Nature mater. 6 (2007) 192-197.
- 64 D.B. Miracle, K.J. Laws, O.N. Senkov and G.B. Wilks; *Metall. Mater. Trans.* 2011, In press.
- 65 D.B. Miracle, D. Louzguine-Luzgin, L. Louzguina-Luzgina and A. Inoue; *Inter. Mater. Rev.*, 55 (2010) 218-256.
- 66 K. Ahn, D. Louca, S.J. Poon, and G.J. Shiflet, Phys. Rev. B 70 (2004) 224103/1-7.
- 67 K.J. Laws, K.F. Shamlaye, K. Wong, B. Gun, M. Ferry; *Metall. Mater. Trans. A* 41A (2010) 1699-1705
- 68 J.H. Xia, J.B. Qiang, Y.M. Wang, Q. Wang, C. Dong; *Mat. Sci. Eng. A*, 449-451 (2007) 281-284.
- 69 N.N. Greenwood, A. Earnshaw, Chemistry of the Elements (2nd ed.), Butterworth-Heinemann, Oxford, UK, 1997.
- 70 B. Cordero, V. Gómez, A.E. Platero-Prats, M. Revés, J. Echeverría, E. Cremades, F. Barragán and S. Alvarez. Covalent Radii Revisited. Dalton Trans., 2008, 2832-2838, doi: 10.1039/b801115j.

## FIGURES

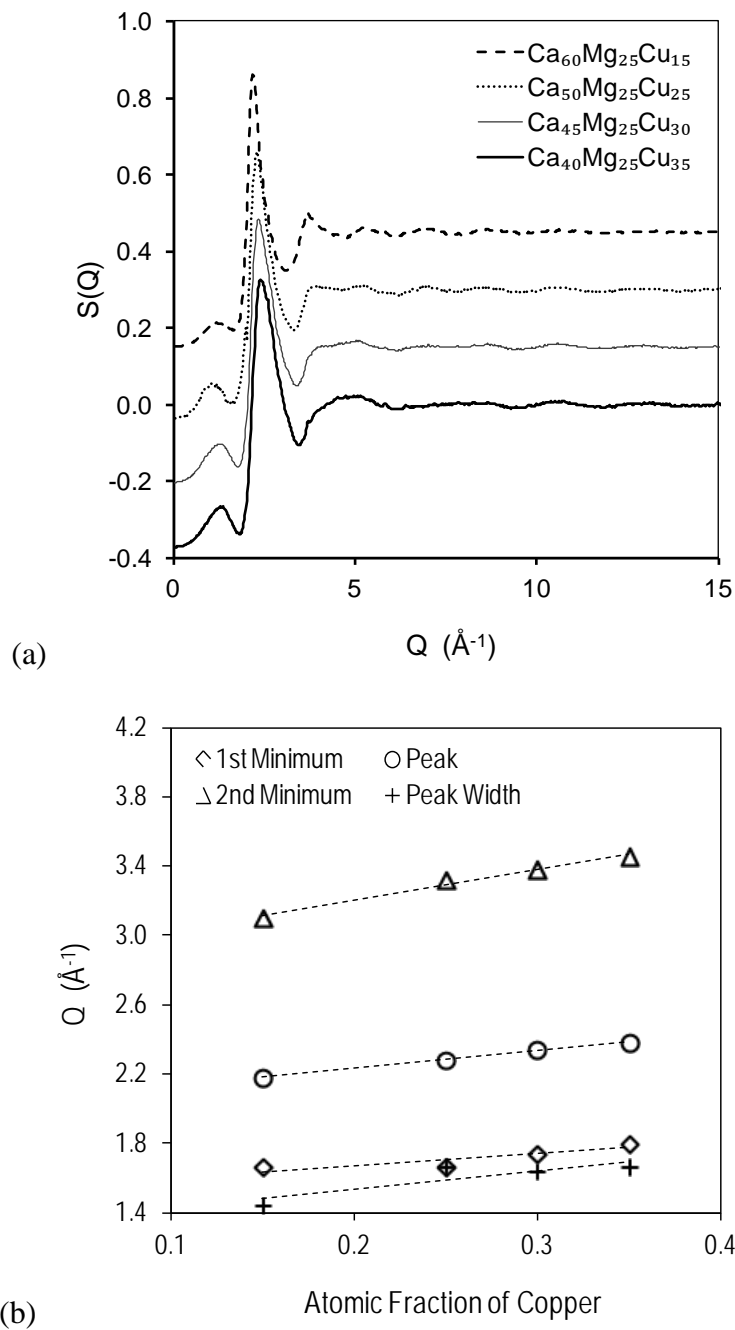


Figure 1. (a) Experimental total neutron scattering structure factors for  $\text{Ca}_{60-X}\text{Mg}_{25}\text{Cu}_{15+X}$  metallic glasses. The curves are separated by shifting along the vertical axis for better view. (b) Dependence on the concentration of copper of the positions of the start (1<sup>st</sup> Minimum), maximum (Peak) and end (2<sup>nd</sup> minimum) of the first peak, as well as the peak width.

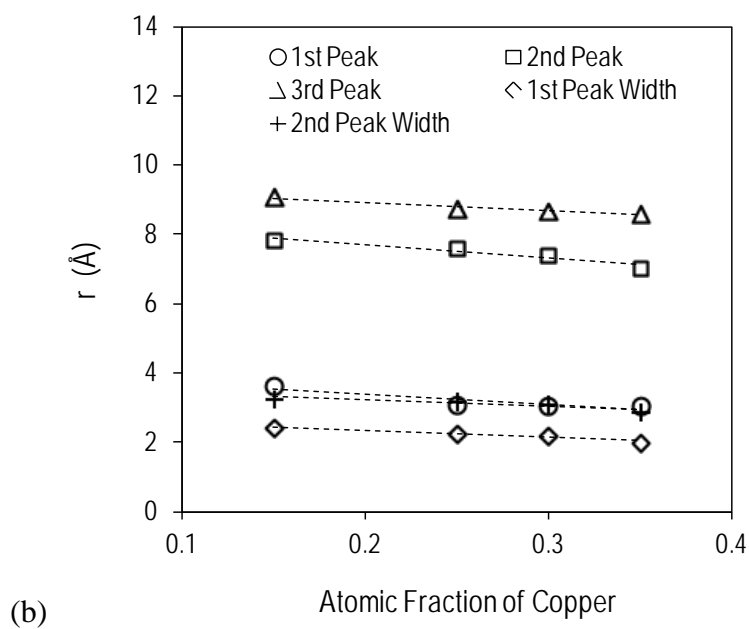
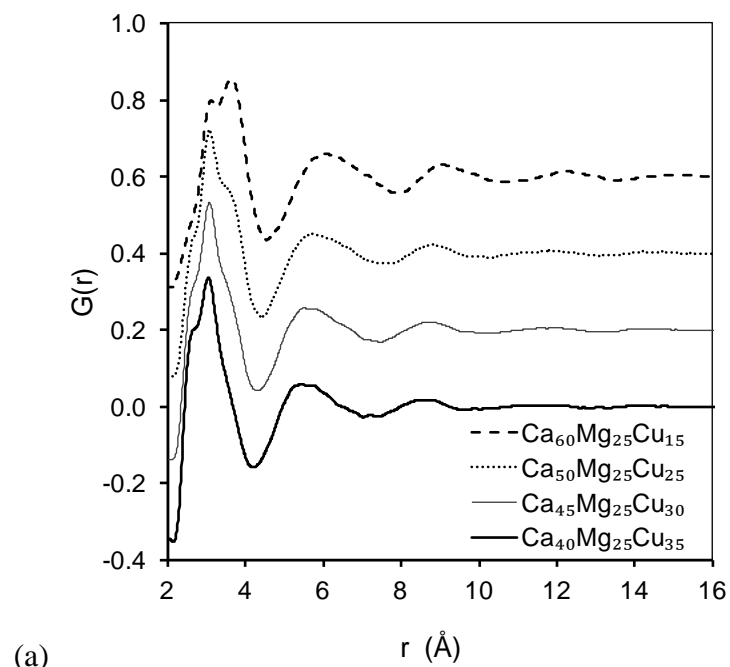


Figure 2. (a) Total radial distribution functions for  $\text{Ca}_{60-x}\text{Mg}_{25}\text{Cu}_{15+x}$  metallic glasses. The curves are separated by shifting along the vertical axis for better view. (b) Dependence on the concentration of copper of the positions of the first, second and third peaks and the width of the first and second peaks.

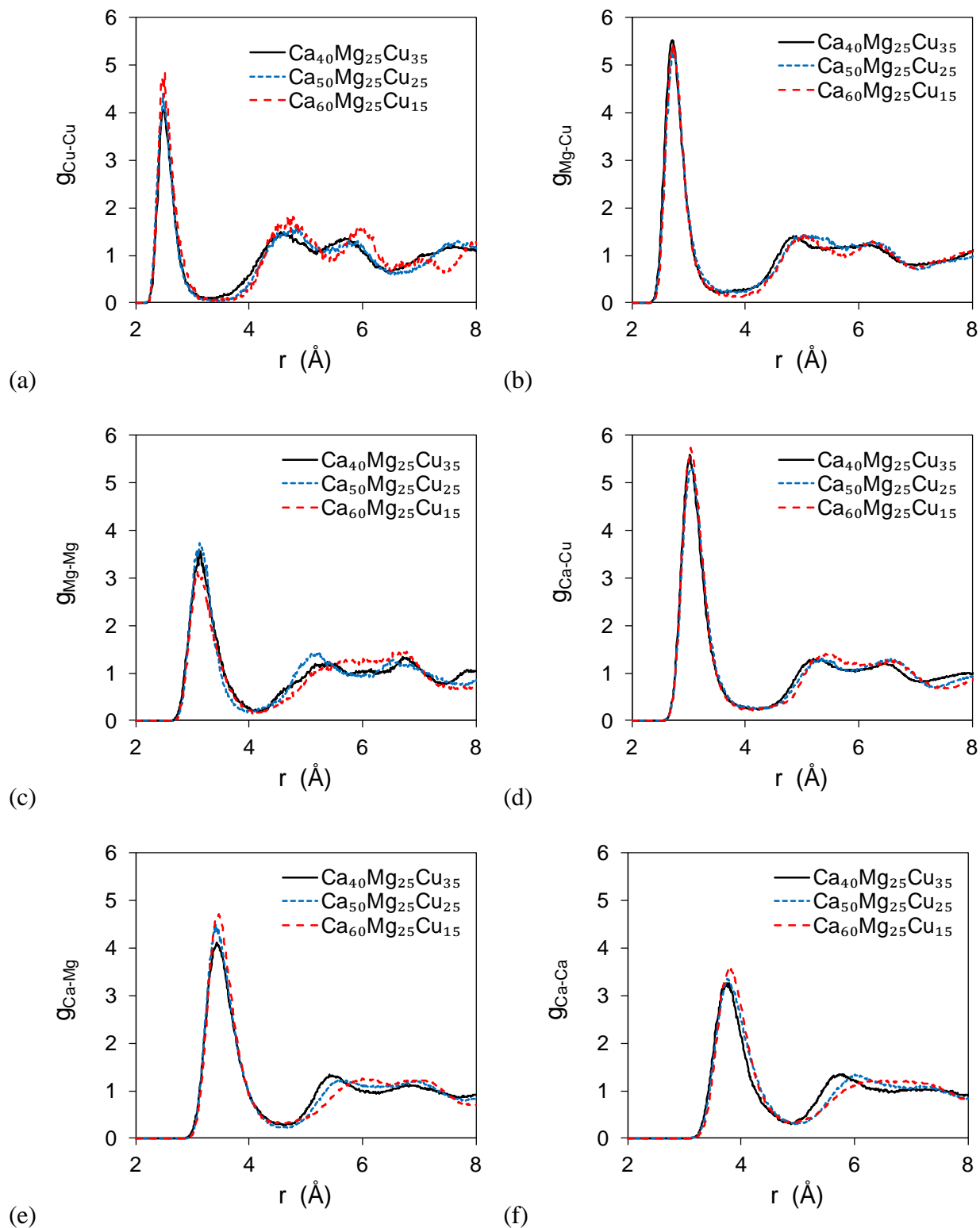


Figure 3. QMD-simulated (a) Cu-Cu, (b) Mg-Cu, (c) Mg-Mg, (d) Ca-Cu, (e) Ca-Mg and (f) Ca-Ca PRDFs for  $\text{Ca}_{40}\text{Mg}_{25}\text{Cu}_{35}$ ,  $\text{Ca}_{50}\text{Mg}_{25}\text{Cu}_{25}$  and  $\text{Ca}_{60}\text{Mg}_{25}\text{Cu}_{15}$  metallic glasses.

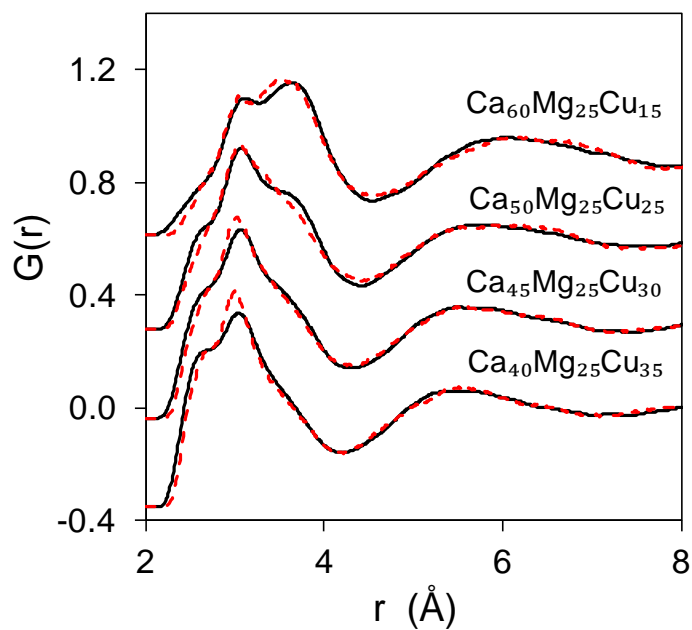


Figure 4. Experimental (dark solid lines) and QMD-simulated (red dashed lines) RDFs for  $\text{Ca}_{60-X}\text{Mg}_{25}\text{Cu}_{15+X}$  metallic glasses. The curves are separated by 0.3-point shifting along the vertical axis for better view.

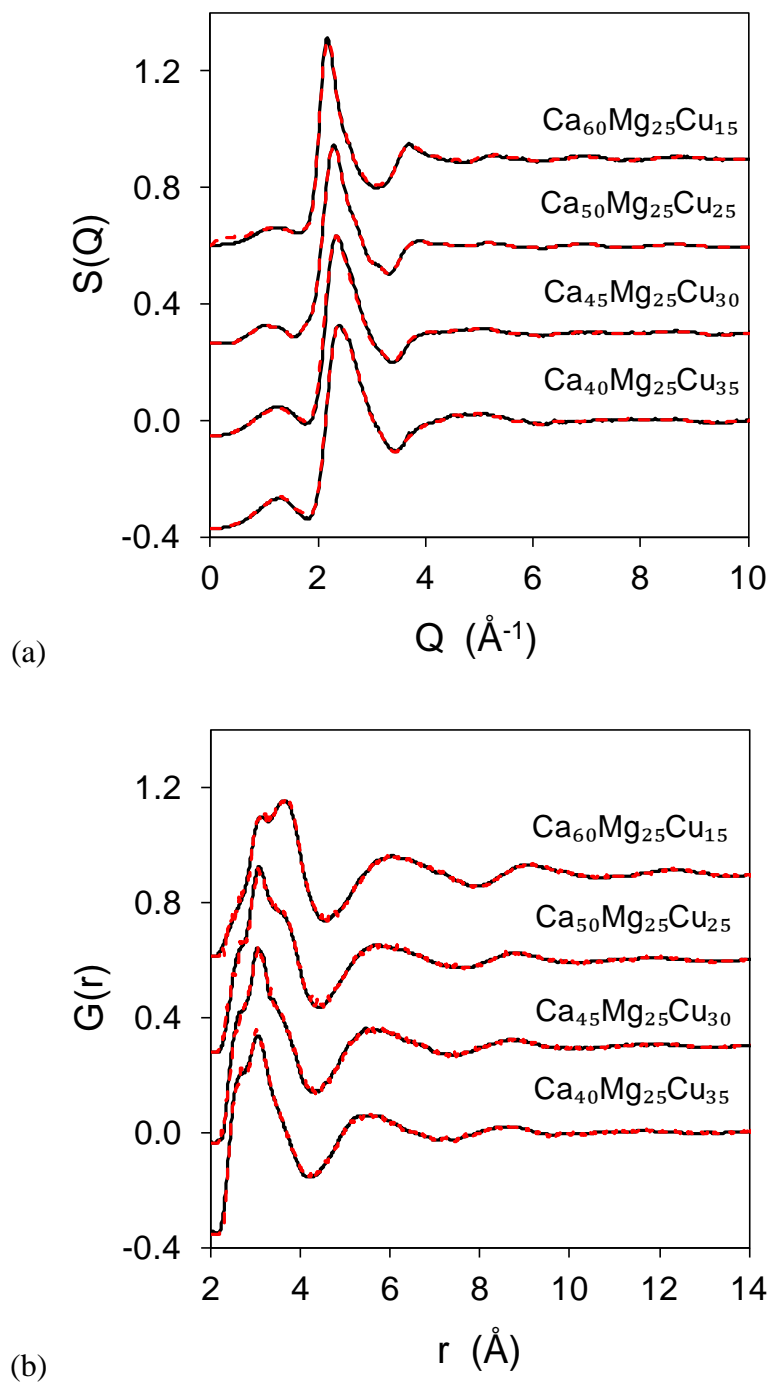


Figure 5. Experimental (dark solid lines) and RMC-simulated (red dashed lines) (a) total structure factors and (b) RDFs for  $\text{Ca}_{60-x}\text{Mg}_{25}\text{Cu}_{15+x}$  metallic glasses. The curves are separated by 0.3-point shifting along the vertical axis for better view.



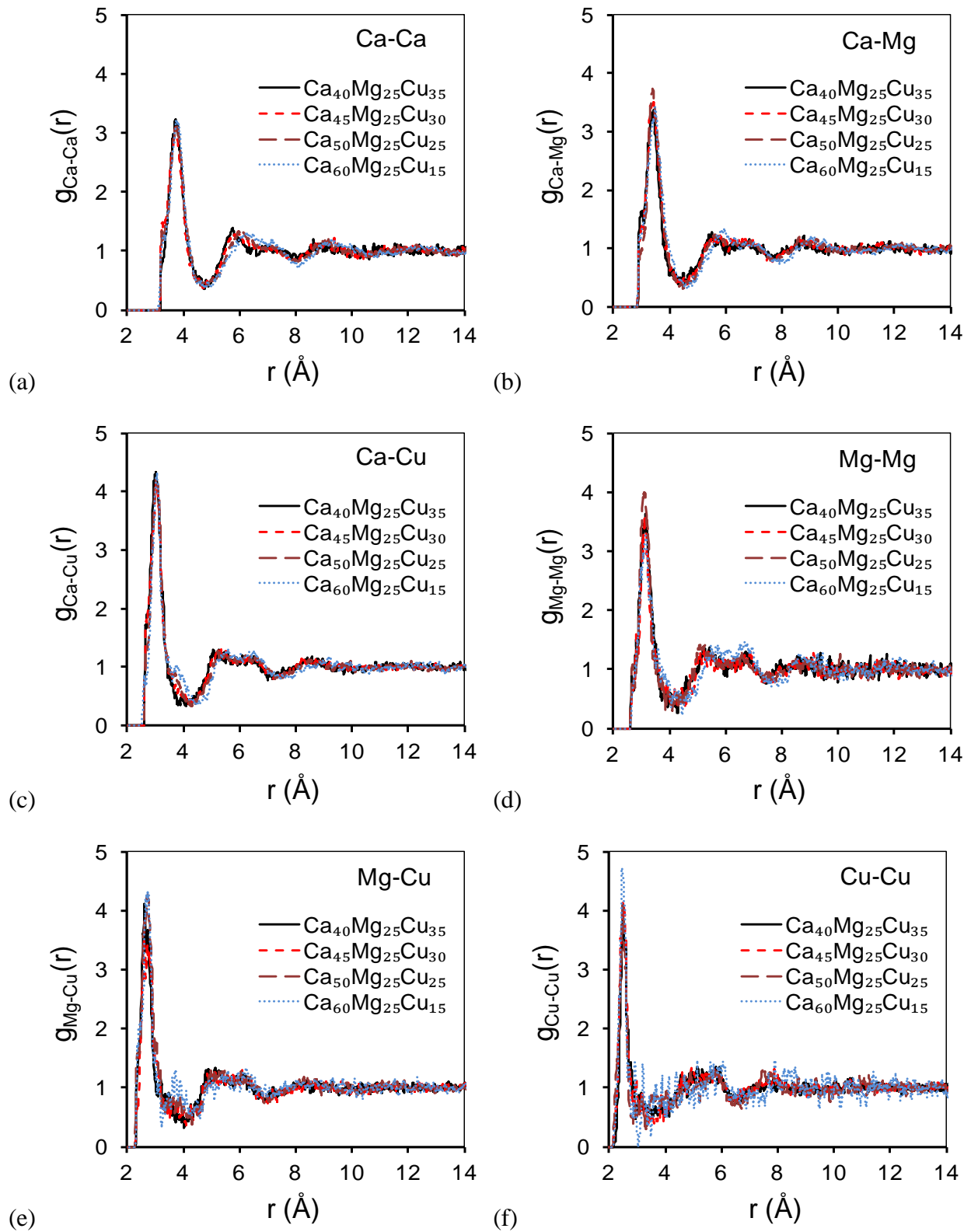


Figure 6. RMC-simulated (a) Ca-Ca, (b) Ca-Mg, (c) Ca-Cu, (d) Mg-Mg, (e) Mg-Cu and (f) Cu-Cu partial radial distribution functions,  $g_{ij}(r)$  for  $\text{Ca}_{60-X}\text{Mg}_{25}\text{Cu}_{15+X}$  metallic glasses.

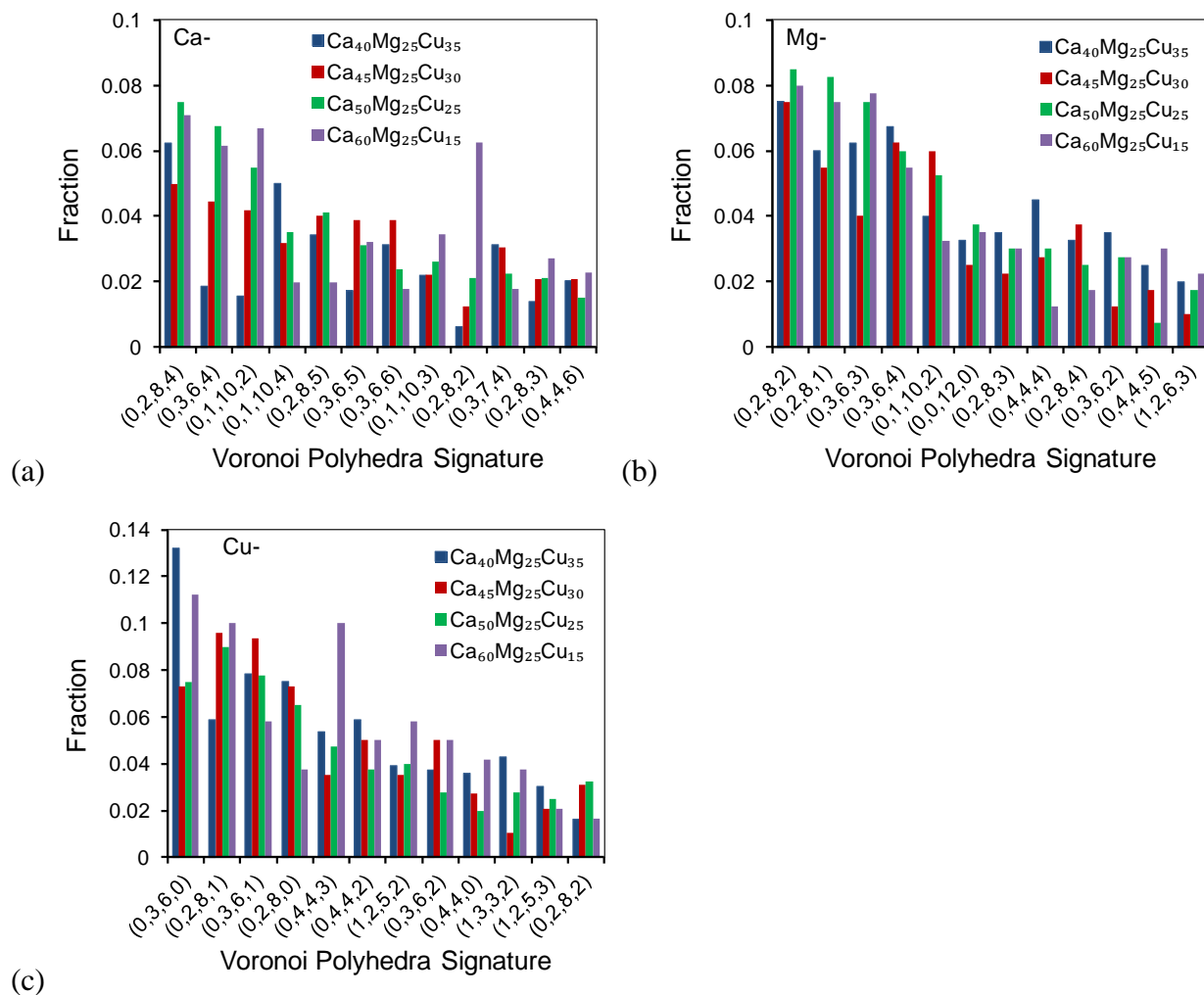


Figure 7. Distribution of different types of (a) Ca-centered (b) Mg-centered and (c) Cu-centered clusters in  $\text{Ca}_{60-x}\text{Mg}_{25}\text{Cu}_{15+x}$  amorphous alloys.

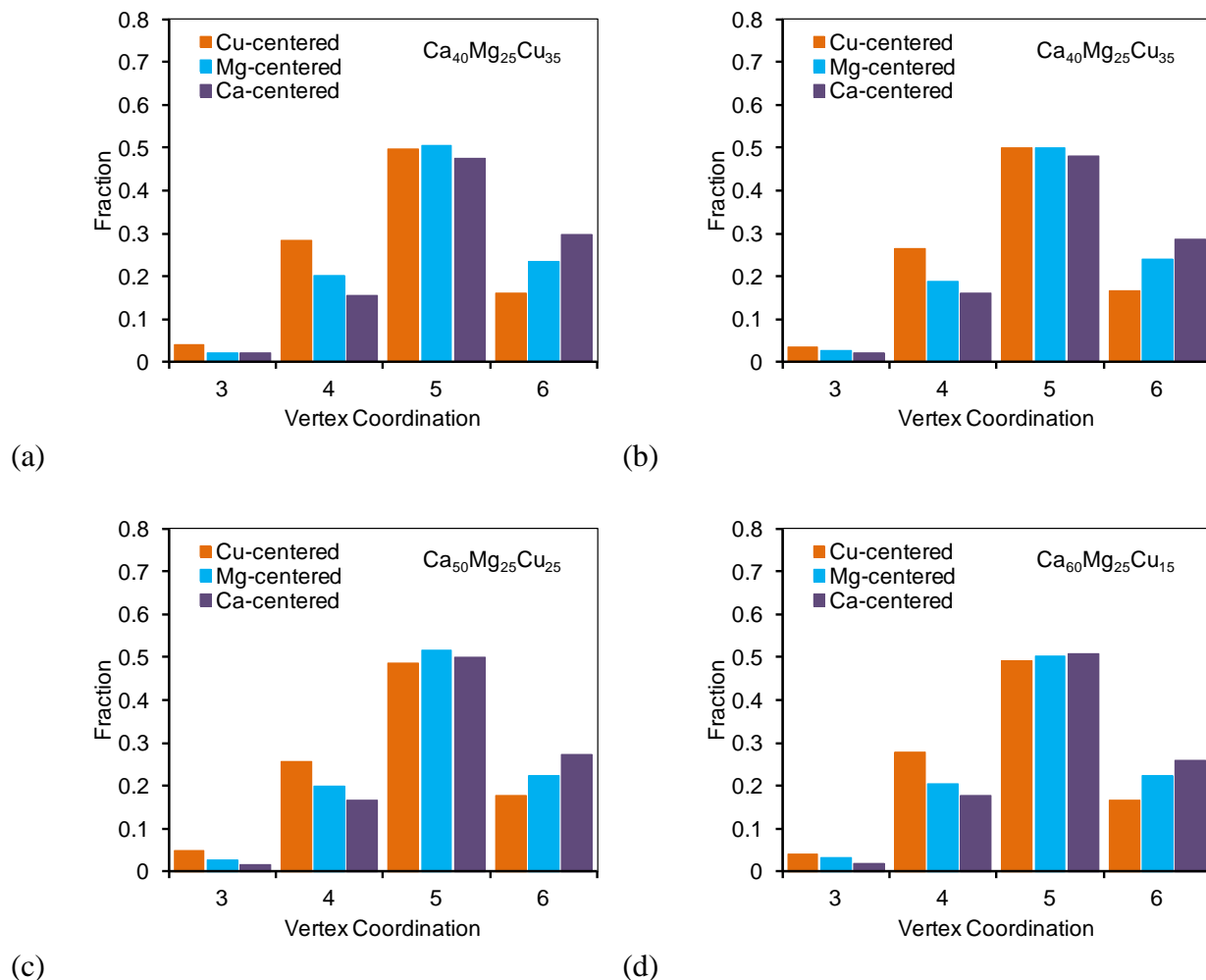


Figure 8. Fractions of 3-, 4-, 5- and 6- coordinated vertices in Ca-, Mg- and Cu- centered clusters in (a)  $\text{Ca}_{40}\text{Mg}_{25}\text{Cu}_{35}$ , (b)  $\text{Ca}_{45}\text{Mg}_{25}\text{Cu}_{30}$ , (c)  $\text{Ca}_{50}\text{Mg}_{25}\text{Cu}_{25}$ , and (d)  $\text{Ca}_{60}\text{Mg}_{25}\text{Cu}_{15}$  amorphous alloys.

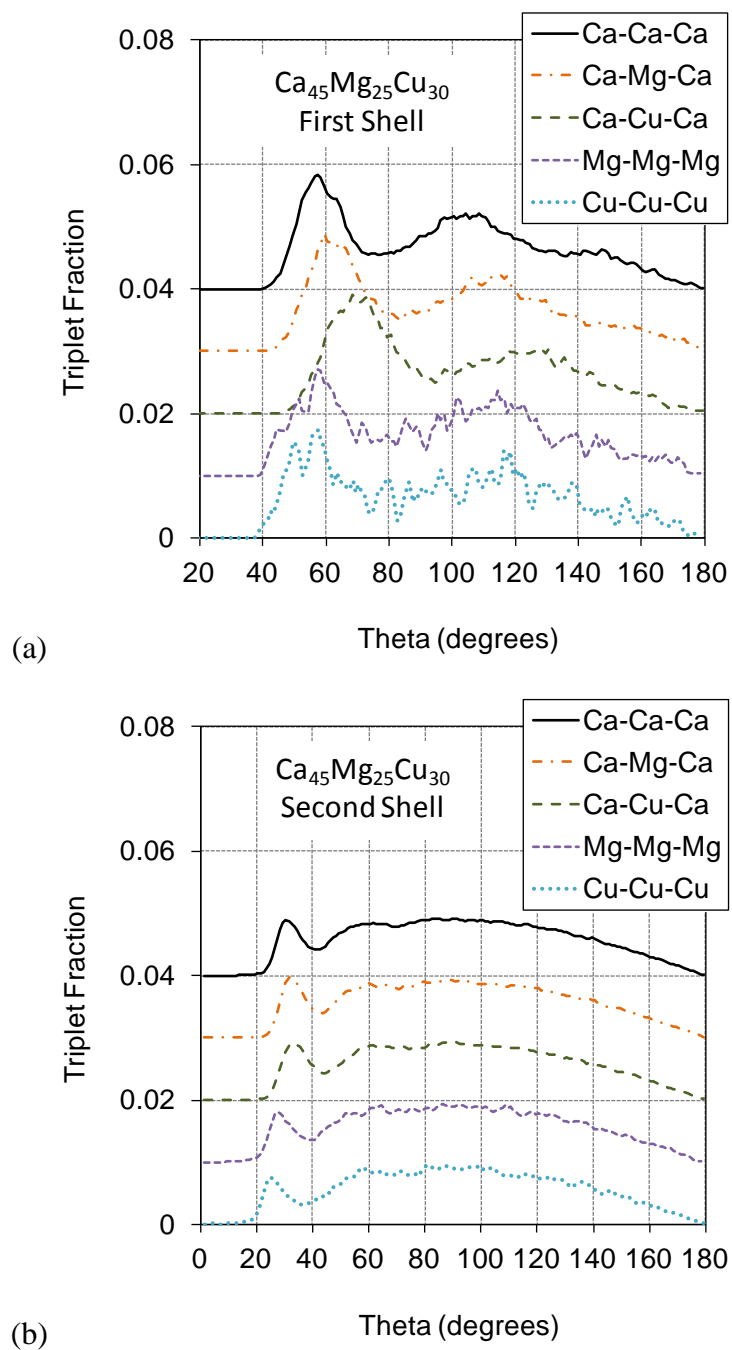


Figure 9. Ca-Ca-Ca, Ca-Mg-Ca, Ca-Cu-Ca, Mg-Mg-Mg and Cu-Cu-Cu bond angle distributions in (a) the first coordination shell and (b) second coordination shell in the  $\text{Ca}_{45}\text{Mg}_{25}\text{Cu}_{30}$  amorphous alloy.

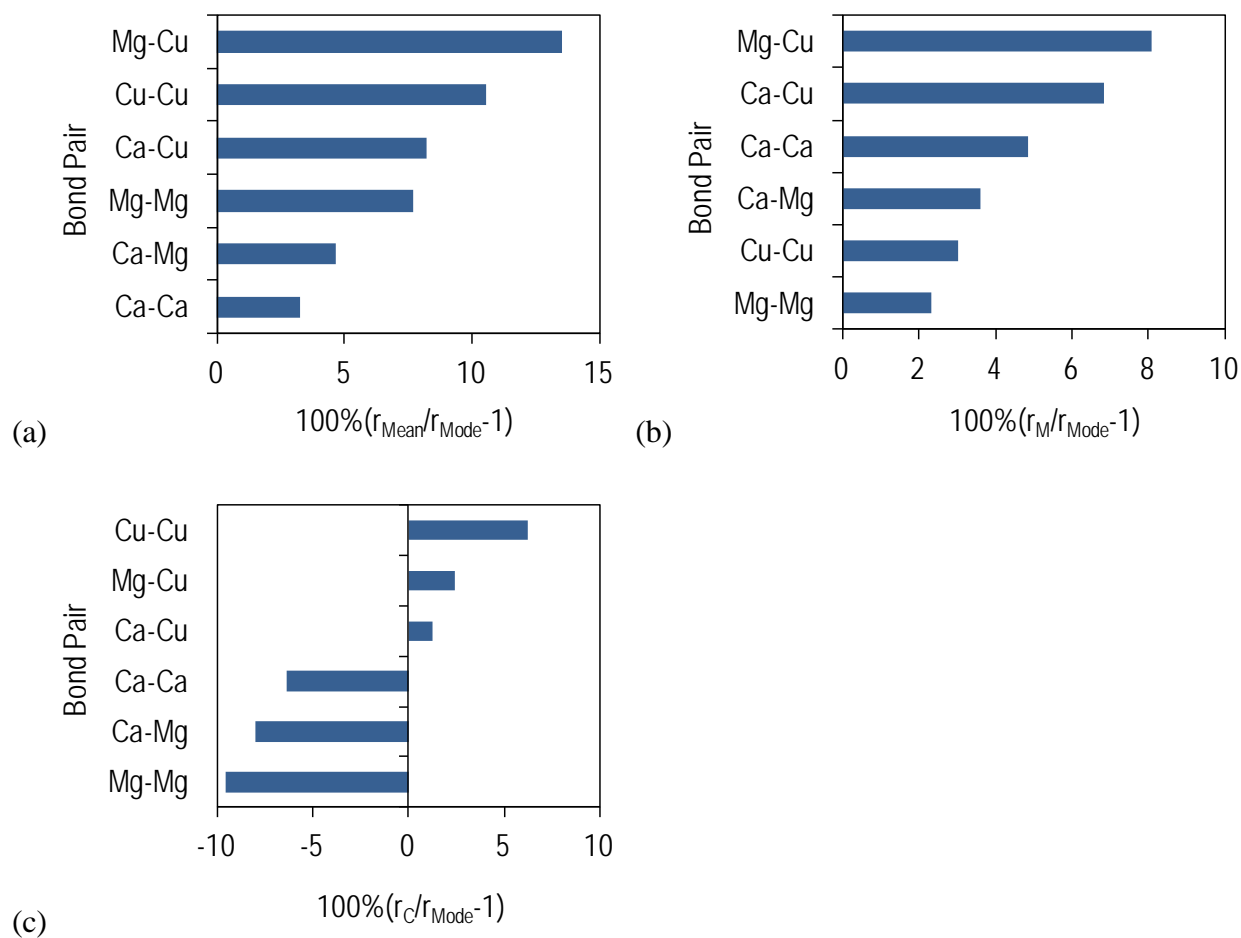


Figure 10. Comparison of the mode atomic pair distances with (a) the respective mean distances in the amorphous structure of the studied Ca-Mg-Cu alloys, and with the reported (b) metallic,  $r_{\text{M}}$ , and (c) covalent,  $r_{\text{C}}$ , bond distances.

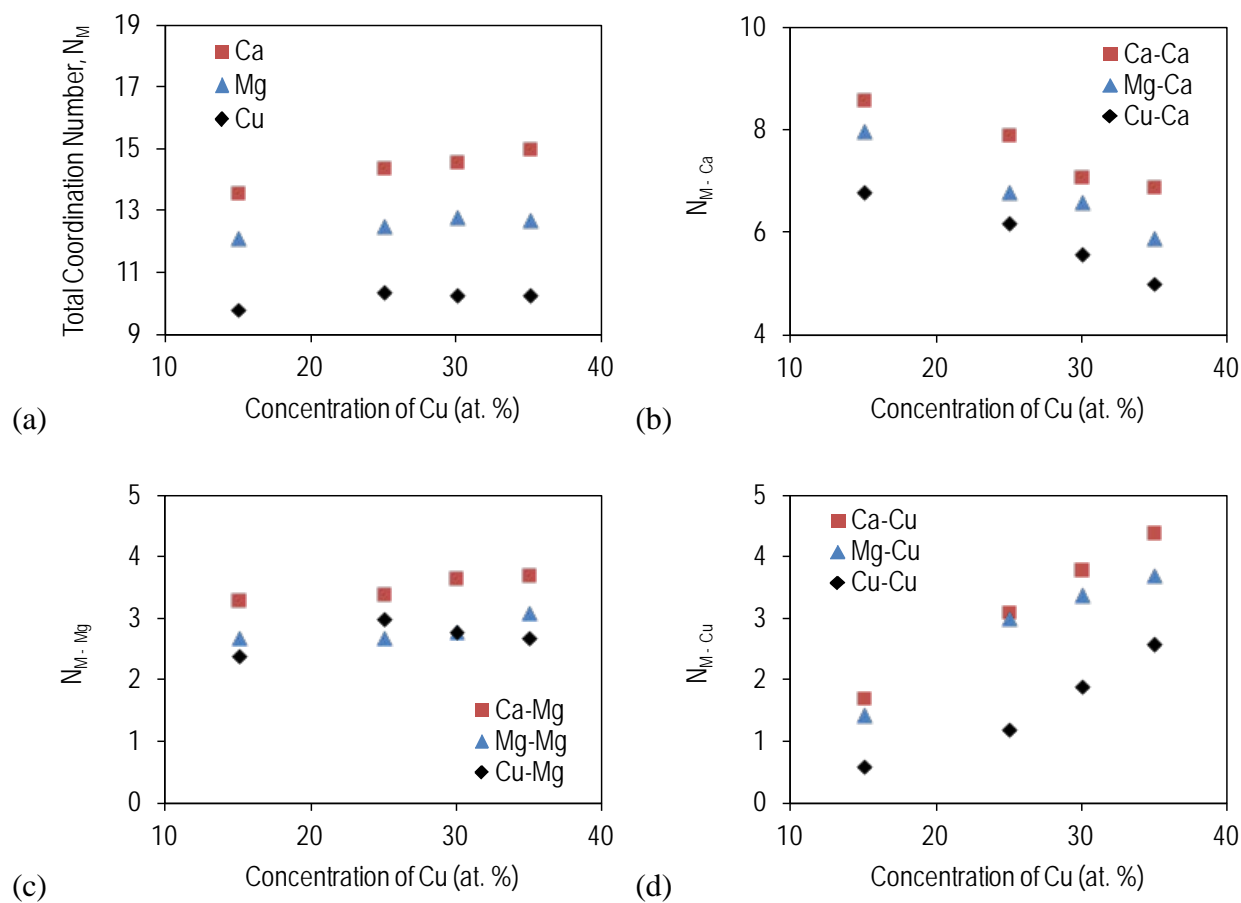


Figure 11. Dependence on the Cu concentration of (a) the total coordination number,  $N_M$ , where M is Ca, Mg, or Cu center atom, and partial coordination numbers (b)  $N_{M-Ca}$ , (c)  $N_{M-Mg}$ , and (d)  $N_{M-Cu}$ .

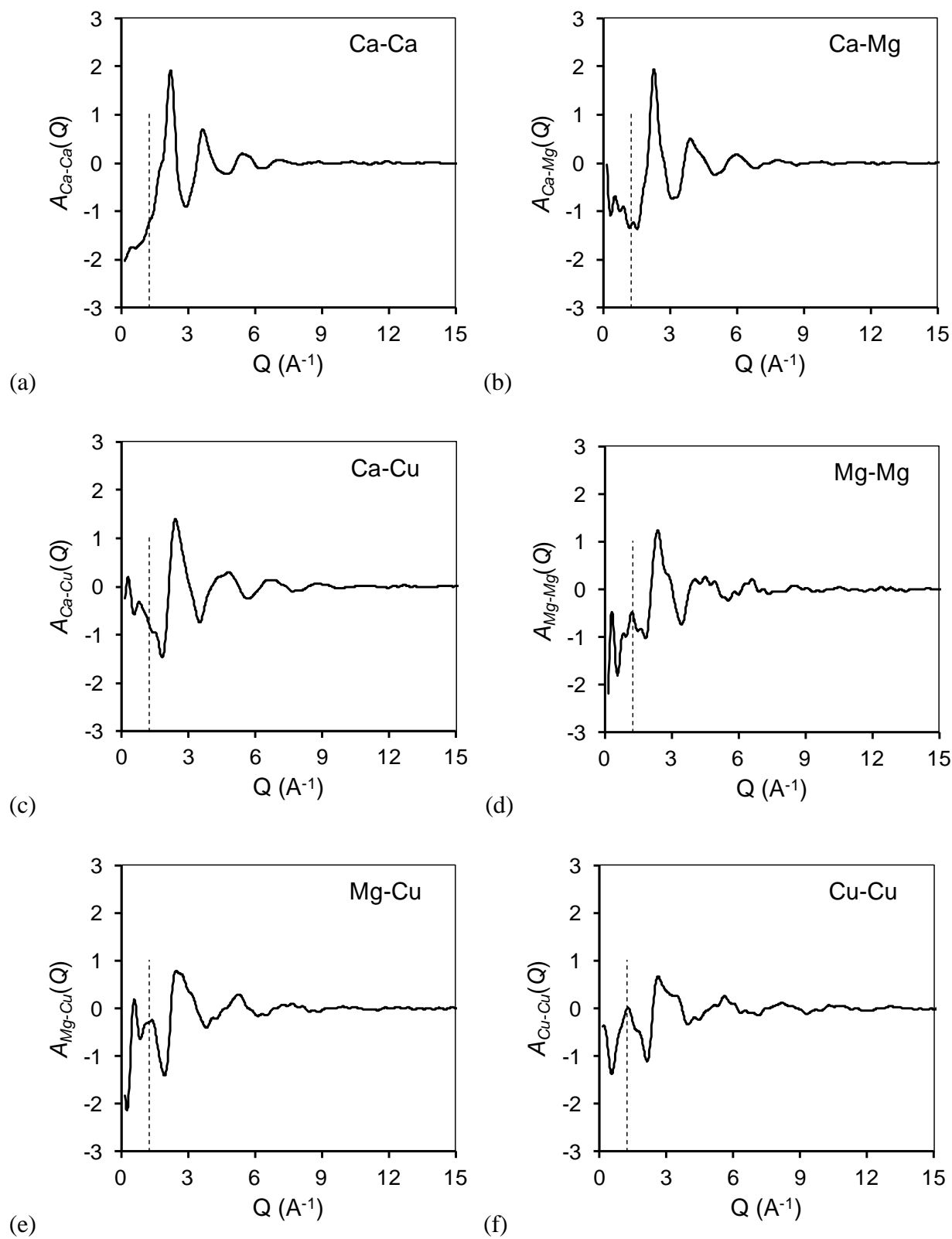


Figure 12. Partial structure factors,  $A_{ij}(Q)$ , for  $\text{Ca}_{45}\text{Mg}_{25}\text{Cu}_{30}$  metallic glass.

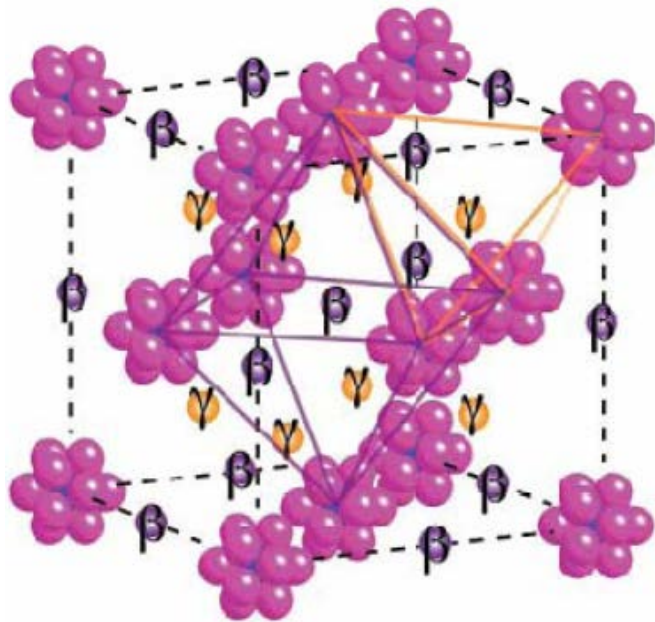


Figure 13. Schematic of a face centered cubic cell formed by Cu-centered clusters (shown by red). Positions of octahedral ( $\beta$ ) and tetrahedral ( $\gamma$ ) interstitial voids are also shown.



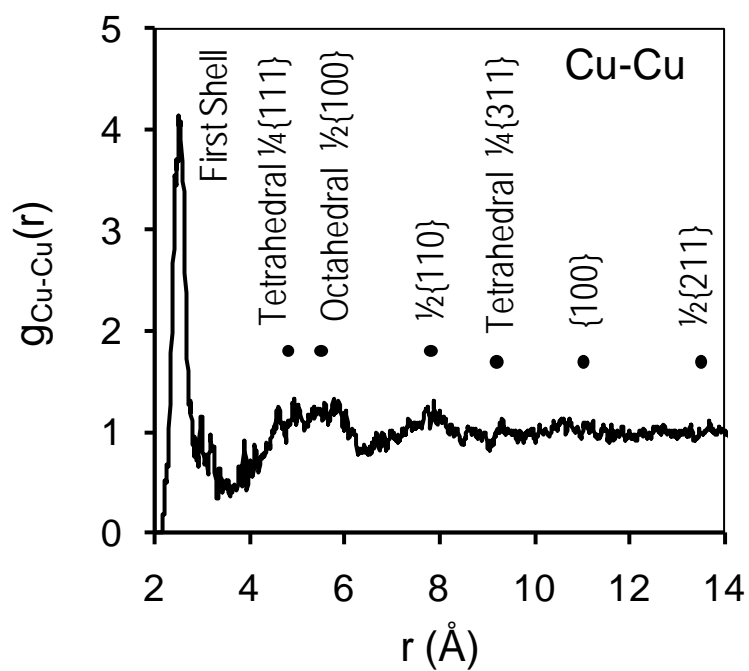


Figure 14. Correlation of the Cu-Cu distances in the FCC super-lattice, formed of the Cu-centered clusters, and the intensity peaks on the Cu-Cu partial radial distribution function.